A SEARCH FOR RARE B DECAYS WITH THE OPAL DETECTOR AT LEP

Research Thesis

Submitted in partial fulfillment of the requirements

for the degree of master of science in physics

Shulamit Moed

SUBMITTED TO THE SENATE OF THE TECHNION -
ISRAEL INSTITUTE OF TECHNOLOGY
TEVET 5763 HAIFA DECEMBER 2002

The research thesis was done under the supervision of Prof. Yoram. Rozen in the department of physics.

I am deeply grateful to Prof. Yoram Rozen for his devoted guidance and support from any geographical distance.

I would like to thank the HEP group at the technion for the friendliness working atmosphere and the kind help in everything that was needed, with special thanks to Hagar Landsman and Amnon Harel.

The help of Dr. Yuval Grossman concerning the theoretical aspects of this work is highly appreciated.

I am thankful to Dr. Helge Voss for the great help and to Pedro Amaral for the cooperation during the time I spent at CERN.

The generous financial help of the Technion is gratefully acknowledged.

Contents

List of Tables

List of Figures

List of symbols and abbreviations

Symbol	Meaning
OPAL	Omni Purpose Apparatus for LEP
LEP	Large Electron Positron Collider
CERN	European Laboratory for Particle Physics (Consil Europeen pour la recherche Nucleaire)
EM	ElectroMagnetism
QCD	Quantum Chromo-Dynamics
SM	Standard Model
MSSM	Minimal Supersymmetric Standard Model
ANN (NN)	Artificial Neural Network (Neural Network)
B $(B^{\pm})$	B (charged) meson
K_s^0 $(ks\bar{h}ort)$	Neutral kaon(anti-kaon), short
K	Kaon
π	Pion
u,c,t,d,s,b	Quarks
$\bar{u}, \bar{c}, \bar{t}, \bar{d}, \bar{s}, \bar{b}$	Anti-quarks
$q(\bar{q})$	Generic symbol for a quark (anti-quark)
$e^-(e^+)$	Electron (Positron)
$\mu^-(\mu^+)$	Muon (anti-muon)
$\tau^-(\tau^+)$	tau (anti-tau)
ν	neutrino
$W^{\pm}$	The weak interaction gauge boson
Z^0	The neutral weak interaction gauge boson
G_F	Fermi constant
E_{vis}	Visible energy
y_{cut}	Principal parameter for a JADE clustering algorithm

Symbol	Meaning
E_i	Energy of particle i
x	The x-axis points horizontally towards the center of LEP
y	The y-axis completes a right-handed Cartesian system with x and z
z	The z-axis lies along the electron beam direction
ϕ	The azimuthal angle, defined relative to the $+x$ axis
dE/dx	Energy loss rate due to ionization
Y	hyper-charge
I	Isospin
V_{CKM}	Cabbibo-Kobayashi-Masakawa matrix
α	Fine structure constant
P_{xy}	Transverse momentum
ϵ_b	Fragmentation model parameter
$C.L$	Confidence Level
BR	Branching ratio

Abstract

A search for the decays $B^- \to K_s^0 K^-$ and $B^- \to \pi^- \pi^- K^+$ was performed using 4.1 million hadronic Z^0 events collected with the OPAL detector at LEP during the years 1989-1995. These decays are strongly suppressed in the Standard Model, but may not be so in models that are extensions of the Standard Model. Therefore these processes provide an appropriate testing ground for physics beyond the Standard Model. In the Standard Model the two decay modes have a branching ratio of the order 10^{-11} or less. The expected branching ratios vary between $10^{-6} - 10^{-9}$ in models like the Minimal Supersymmetric Standard Model with and without R-parity conservation or the two Higgs doublet model.

The search for these decays was done by reconstructing B meson candidates by combining tracks using different selection criteria based on event variables measured by the detector and artificial neural network classifications.

In agreement with other searches for these decays done by the CLEO collaboration and the BELLE collaboration, no evidences for a signal are observed and at 90% confidence level an upper limit of $2.1 \cdot 10^{-4}$ is set on the branching ratio of the decay $B^- \to \pi^- \pi^- K^+$ and an upper limit of $7.8 \cdot 10^{-5}$ on the branching ration of the $B^- \to K_s^0 K^-$ decay.

Chapter 1

Introduction

Particle physics is the study of the basic elements of matter and the forces acting among them. It aims to determine the fundamental laws that control the make-up of matter and the physical universe.
The Standard Model is a theory that describes how the different elementary particles are organized and how they interact with each other by means of the different forces.
Mathematically the Standard Model is the gauge group $SU(3)_C \otimes SU(2)_L \otimes U(1)_Y$ that spontaneously breaks to the $SU(3)_C \otimes U(1)_{EM}$ gauge group. The elementary particles are split up into quarks and leptons, as shown in table 1.1. Both consist of six fields that split into three generations, with the first generation being the lightest,and the third the heaviest. Both the leptons and the quarks can carry electrical charge, while only the quark carries a color charge that is associated with the strong interaction. A bound system of quarks is called a hadron. All hadrons are color-neutral objects, but may carry electric charge. Furthermore, there are different force carrying particles which lead to the interactions between particles, these are called gauge bosons.

The four known forces in nature are: gravity, the electromagnetic force, the strong force, the weak force.

The Standard Model describes the electromagnetic, the strong and the weak interactions. Due to its weakness, gravity, which is not included in this model, has negligible effects in elementary particle interactions. In the Standard Model the photon mediates the electromagnetic interactions, the gluon carries the strong force, and the W and Z bosons transmit the weak force.

generation	I	II	III	gauge bosons
Quarks	u	c	t	g gluons
	d	s	b	γ photon
Leptons	ν_e	ν_μ	ν_τ	$W^{\pm}$
	e	μ	τ	Z^0

Table 1.1: Summary of the SM particles.

1.1 Electroweak Interactions

The Standard Model of the electroweak theory is based on the gauge group $SU(2)_L \otimes U(1)_Y$. The $SU(2)$ represents weak isospin symmetry, and the $U(1)$ represents the hypercharge - Y. The hypercharge is a linear combination of the electric charge and the weak isospin and is not conserved in weak interactions. It has been experimentally shown (at low energies) that only particles with negative helicity ('left handed ') can interact through the weak interaction, and therefore the fermions are divided into left handed doublets and right handed singlets under $SU(2)$.

The quark mass eigenstates are different from the quarks weak eigenstates. The Cabbibo-Kobayashi-Masakawa (CKM) matrix is the transformation between the mass eigenstates

$$\begin{pmatrix} u \\ d \end{pmatrix} \begin{pmatrix} c \\ s \end{pmatrix} \begin{pmatrix} t \\ b \end{pmatrix}$$

and the weak interaction quark eigenstates

$$\begin{pmatrix} u \\ d' \end{pmatrix} \begin{pmatrix} c \\ s' \end{pmatrix} \begin{pmatrix} t \\ b' \end{pmatrix}$$

in the form:

$$\begin{pmatrix} d' \\ s' \\ b' \end{pmatrix} = \begin{pmatrix} V_{ud} & V_{us} & V_{ub} \\ V_{cd} & V_{cs} & V_{cb} \\ V_{td} & V_{ts} & V_{tb} \end{pmatrix} \begin{pmatrix} d \\ s \\ b \end{pmatrix}$$

Each matrix element measures the coupling between a pair of quarks. The strength of the quark coupling, i.e - the elements of the CKM matrix, are shown bellow [1]:

$$V_{CKM} = \begin{pmatrix} 0.9742 - 0.9757 & 0.2219 - 0.226 & 0.002 - 0.005 \\ 0.219 - 0.225 & 0.9734 - 0.9749 & 0.037 - 0.043 \\ 0.004 - 0.014 & 0.035 - 0.043 & 0.9990 - 0.9993 \end{pmatrix}$$

Why B? The fifth of the six known types of quark, the b quark is commonly referred to as the beauty or bottom quark. A key factor in the experimental interest in b physics is the potential insight it affords into physics at very short distances. In particular, it is hoped that the high precision study of phenomena such as CP violation, rare decays and flavor changing processes will provide hints of new interactions associated with the flavor sector of whatever theory lies beyond the Standard Model. However, while the object of study is the b quark, it is bound by strong interactions into color neutral hadrons. Therefore experimentally we deal with B mesons (a bound system of quark and anti-quark, where one of them is a b or a $\bar{b}$).
The result is an interplay between theory and experiment, where one often cannot measure what one can compute reliably, nor compute reliably what one can measure.

Chapter 2

Motivation

The intensive search for physics beyond the Standard Model is being done nowadays in various areas of particle physics. Among these rare B meson decays are suggested to give good opportunities for discovering new physics beyond the Standard Model. Recently, it has been suggested [2] to investigate effects of new physics possibly arising from $b \to ss\bar{d}$ or $b \to dd\bar{s}$ decays. This search is performed in order to set an upper limit on the following two decays: [1]

- $B^- \to \bar{K}^0 K^-$, which is mediated by the quark transition $b \to ss\bar{d}$, and $B^- \to K^0 K^-$ which is mediated by the quark transition $b \to s\bar{s}d$.
  The observable process here is $B^- \to K_s^0 K^-$.

- $B^- \to \pi^- \pi^- K^+$, which is mediated by the quark transition $b \to dd\bar{s}$.

2.1 Branching Ratio Estimations in the Standard Model

The $b \to ss\bar{d}$ transition is mediated in the Standard Model by a box diagram with the up-type quarks and the weak bosons inside the loop (figure 2.1). A simple estimation according to the theory of weak interaction predicts the

---

[1] Charge conjugation is assumed throughout these analyses.

following branching ratio for the channel $b \rightarrow s s \bar{d}$ in the Standard Model [2]:

$$\Gamma = \frac{m_b^5}{48(2\pi)^3} \left| \frac{G_F^2}{2\pi^2} m_W^2 V_{tb} V_{ts}^* [V_{td} V_{ts}^* f(\frac{m_W^2}{m_t^2}) + V_{cd} V_{cs}^* \frac{m_c^2}{m_W^2} g(\frac{m_W^2}{m_t^2}, \frac{m_c^2}{m_W^2})] \right|^2 , \tag{2.1}$$

where

$$f(x) = \frac{1 - 11x + 4x^2}{4x(1-x)^2} - \frac{3}{2(1-x)^3} ln(x) \tag{2.2}$$

$$g(x,y) = \frac{4x-1}{4(1-x)} + \frac{8x - 4x^2 - 1}{4(1-x)^2} ln(x) - ln(y) \tag{2.3}$$

m_q is the quark mass, q=b,c,t
m_W is the W gauge boson mass
G_F is the Fermi coupling constant

This calculation turns out to give an exceedingly small rate in the Standard Model. Due to the strong GIM suppression and the small CKM angles involved, the W-box contribution is tiny and the process is highly suppressed. The branching ratio is less than 10^{-11}, far beyond the ability of OPAL, considering the amount of data that was collected. The predicted branching ratios will not change greatly even if QCD corrections and the kinematic dependent contribution, which is smaller than 10% in the term proportional to $\frac{m_c^2}{m_W^2}$, are included.

2.2 Branching Ratio Predictions in Other Models

Although the branching ratio predictions of the rare decays $B^- \rightarrow K_s^0 K^-$ and $B^- \rightarrow \pi^- \pi^- K^+$ are so small within the Standard Model, they may be greater in other models. In the Minimal Supersymmetric Standard Model (MSSM) [2] this transition can be induced by the squark-gaugino (or higgsino) box diagram at a level of $10^{-7} - 10^{-8}$. An alternative mechanism for this channel

in supersymmetric models is through R-parity violating couplings [2]. These two possibilities appear to be the only ones that will produce significant enhancement of these decays within supersymmetric models. Two higgs doublet models could also induce these decays at branching ratios significantly larger than in the Standard Model, for a certain range of parameters involved.
The decay $B^- \rightarrow K_s^0 K^-$ has a K_s^0 in the final state. This complicates the possibility to detect the process $b \rightarrow ss\bar{d}$ because of $K^0 - \bar{K}^0$ mixing. The process $B^- \rightarrow K^0 K^-$ can not be experimentally separated from the process $B^- \rightarrow K_s^0 K^-$ mediated by the quark transition $b \rightarrow s\bar{s}d$, which is a pure penguin process.
The decay $B^- \rightarrow K^- K^- \pi^+$ has the same quark transition as in the decay $B^- \rightarrow K^0 K^-$. A search for this decay was done in OPAL [3] and set the upper limit to be $8.8 \cdot 10^{-5}$. A later search done by the BELLE collaboration [4] set the upper on $B^- \rightarrow K^- K^- \pi^+$ to be $3.2 \cdot 10^{-6}$.
However, the theoretical estimations [2] show a significant differences in the branching ratio estimations between the Standard Model and its extension models, and therefore the decay channel $B^- \rightarrow K_s^0 K^-$ can also serve as an opportunity to search for this rare quark transition.

The quark transition $b \rightarrow dd\bar{s}$ is driven by the same mechanism within the Standard Model, but is even more suppressed due to the smaller CKM angles involved.

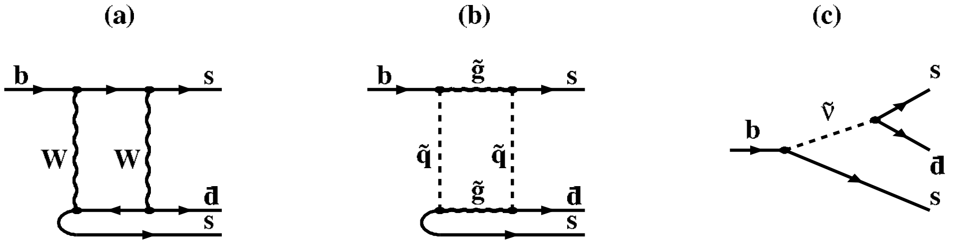

Figure 2.1: $b \rightarrow ss\bar{d}$ transition (a) SM, (b) MSSM, (c) MSSM with R-parity violating coupling.

2.3 Existing Results

$\underline{B^- \rightarrow K_s^0 K^-}$

In October 2001 (after this search with the OPAL data had begun) the BaBar collaboration reported their results from the search for the decay $B^- \rightarrow K_s^0 K^-$ [5]. They set the upper limit on the branching ratio to be $2.6 \cdot 10^{-6}$ - one order of magnitude better than the result achieved in this search. The main goal of the BaBar collaboration is to study phenomena like CP asymmetries in the decays of neutral B mesons and to measure sensitively the CKM matrix element V_{ub}, along with other B meson related measurements. The experiment is designed to produce B mesons from e^+e^- collisions and therefore had much more statistics for making this search ($\sim 23 \cdot 10^6$ events). In addition it is capable of identifying K_L^0 and neutral pions.

$B^- \rightarrow \pi^- \pi^- K^+$

This decay mode was analysed by the CLEO collaboration in 1996 [6], where the upper limit on the this branching ratio was set to be $5.6 \cdot 10^{-5}$.
In June 2002 the Belle collaboration published their result for this search [7], where they achieved an upper limit on the branching ratio of $7 \cdot 10^{-6}$, $45.3 \cdot 10^6$ $B\bar{B}$ pairs were used for the Belle analysis.

Chapter 3

The OPAL Experiment

3.1 LEP

The LEP (Large Electron Positron) accelerator at CERN was the largest collider in the world. The LEP ring is 27 km in circumference and buried about 100 meters underground, where bunches of electrons and positrons raced around in opposite directions, as they are accelerated to almost the speed of light. At four symmetric points around the ring the bunches are focused down and made to collide at the heart of the four LEP experiments -ALEPH, L3, DELPHI and OPAL (figure 3.1). Each bunch contains more than a hundred thousand millions particles, but on average only one in about 40,000 collisions between the bunches produces the desired effect - a head-on electron-positron collision. Each bunch travels around the ring more than 10,000 times a second.
LEP began operating in the summer of 1989, with center of mass energy tuned exactly to the value needed to produce the electro-weak gauge boson Z^0. At the end of 1995 the center of mass energy was increased to almost double its earlier value. In the summer of 1996, LEP ran at the exact value needed to produce pairs of the charged weak bosons W^+ and W^-. The energy was gradually increased up to 207 GeV and the LEP collider operation ended in November 2000.

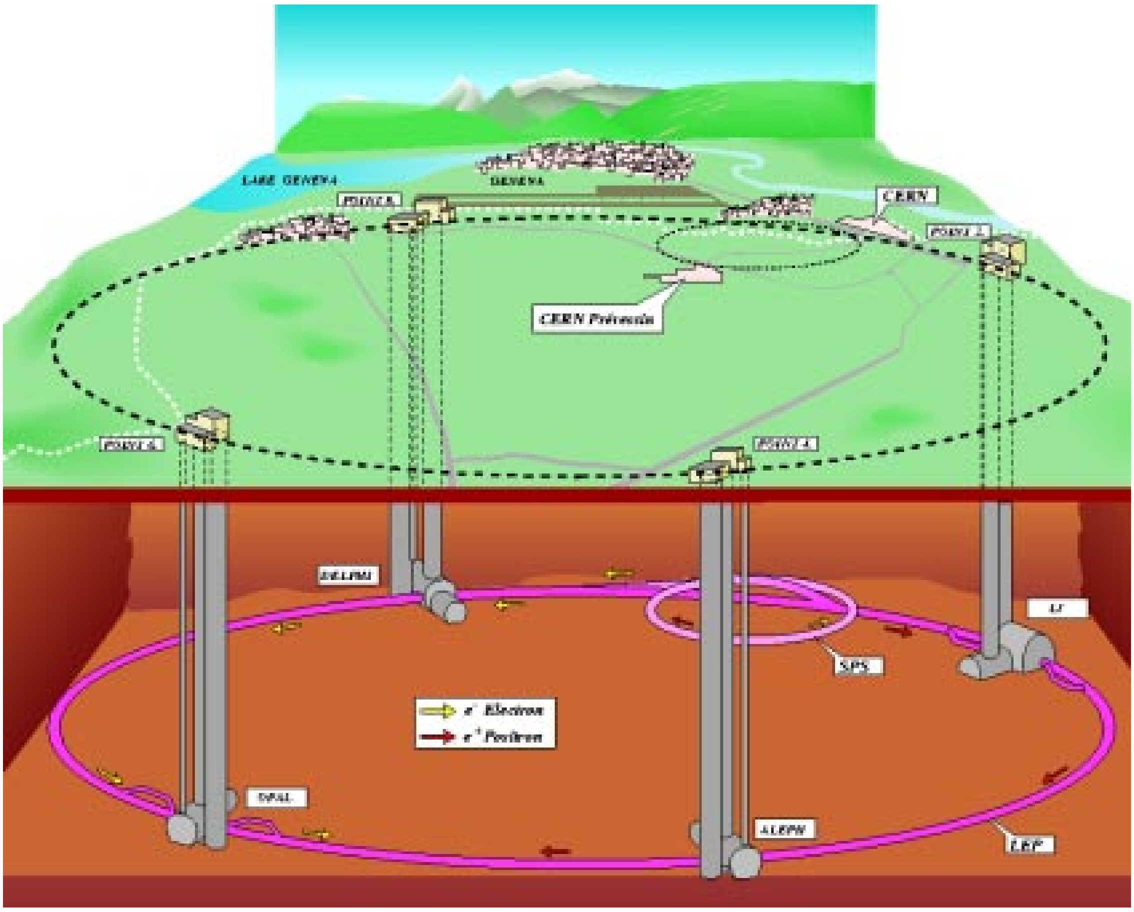

Figure 3.1: A view of the LEP tunnel and location of the four detectors.

3.2 The Detector

The OPAL (Omni Purpose Apparatus for LEP) detector was a large, multipurpose, particle detector for the LEP collider. The components of the detector were arranged outside the beam pipe, in a layered structure.

The OPAL coordinate system is a 3-dimensions Cartesian Coordinate System whose origin is at the nominal interaction point and the z-axis along the nominal electron beam direction (this is anti-clockwise around LEP when viewed from above). The x-axis is horizontal and directed towards the center of LEP, and the y-axis is normal to the z-x plane. Since the z-axis is inclined by 1.39% with respect to the horizontal, it follows that the y-axis will be similarly inclined with respect to the vertical. The coordinate system together with the detector components can be seen in figure 3.2.

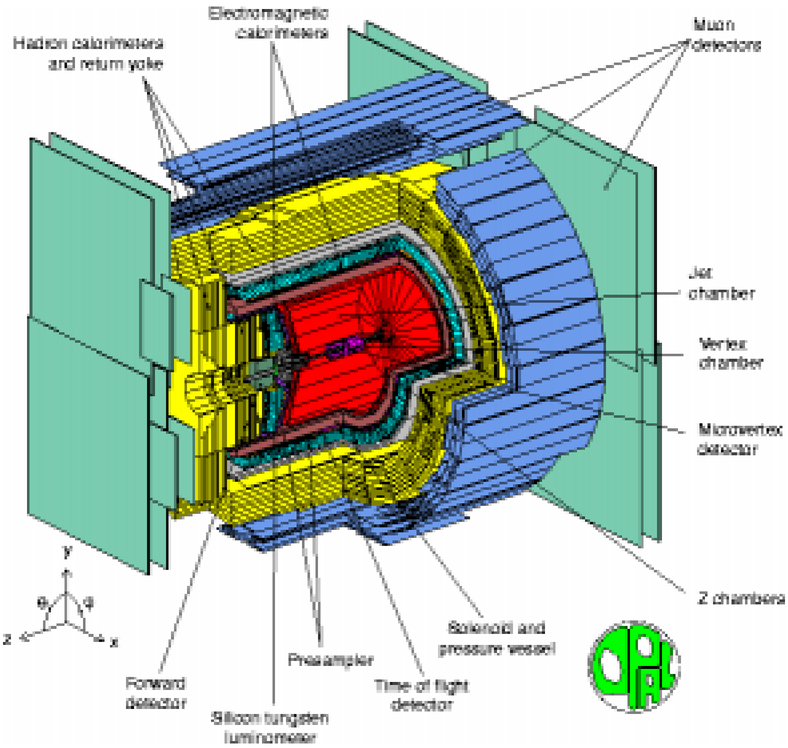

Figure 3.2: Schematic view of the OPAL detector.

3.2.1 Beam Pipe

Since the beam pipe must be able to keep a high level of vacuum inside (being a part of LEP vacuum chamber) while coping with 4 bar outside (see section 4.2.2), it consists of two axial tubes. In the 1.1 mm thick beryllium inner pipe, with a minimum inner radius of 53 mm, exists the vacuum. The outer pipe, which is made of a 2 mm think carbon fiber epoxy composite with an inner radius of 80 mm, holds the 4 bar gas pressure of the surrounding central detector.
The space between the two pipes is used by the silicon microvertex detector.

It is important that the material of the beam pipe has a good radiation length transparency. The amount of material in the beam pipe was about 1.2% radiation length.

The detector is made up of three main layers, each of which is further subdivided. The sub-detectors are summarized in table 3.1. A cut through the planes parallel and perpendicular to the beam axis showing the sub-detectors is shown in figure 3.3.

3.2.2 The Tracking System

The tracking system of OPAL includes low-density devices, positioned inside a solenoid which provides a uniform magnetic field of 0.435 Tesla. In the r-ϕ plane the resolution is found to be 75 μm and in the $r - z$ plane it is 2 mm.

Silicon Microvertex Detector

At the beginning of LEP operation, the OPAL detector had no silicon detector as part of the vertexing system. The first OPAL silicon microvertex detector was installed in June 1991, and had one coordinate readout (ϕ only). It consisted of two concentric layers of single-sided silicon detectors with AC coupled readout strips at 50 μm pitch oriented for azimuthal (ϕ) coordinate measurements, and had a single hit resolution of 8 μm. The inner layer covers a polar angle range of $|cos\theta| < 0.83$ and the outer layer covers $|cos\theta| < 0.77$. The use of the silicon microvertex information resulted in a large improvement in tracking for OPAL. In 1993 the vertex silicon detector was upgraded for obtaining the second (z) coordinate information. The new detector obtained ϕ and z coordinate readout using back-to-back single-sided AC coupled silicon strip detectors. The intrinsic single-hit resolution at normal incidence are about 5 μm in ϕ and about 13 μm in z for particles trajectories normal to the plane of the detectors. The resolution in ϕ is unchanged as a function of polar angle, while the resolution in z degrades to about 15 μm at 30° and further to about 20 μm at 45°.
The importance of the silicon vertex detector is in its improvement of the vertexing system. It enables a more precise reconstruction of decay vertices, especially of particles with a short lifetime such as B mesons.

Central Vertex Detector

The vertex detector, located between the beam-pipe and the jet-chamber, is used to locate decay vertices of short-lived particles and to improve the momentum resolution. It is a 1 m long, 0.47 m diameter cylindrical drift chamber which is segmented radially into an inner layer of 36 cells with axial wires and an outer layer of 36 small angle (4 degree) stereo cells. The axial cells provide a precise measurement of the position (50 microns) in the r-ϕ plane. A coarse measurement of the z-coordinate can be made by measuring the time difference between the signals from the two ends of the anode wire. The combination of axial and stereo cell information provides a precise z measurement for charged particles close to the interaction region.

Jet Chamber

The jet-chamber records tracks of charged particles over almost the entire solid angle. It measures their momenta through the bending due to a magnetic field. Particle identification is done by multiple sampling of the energy loss in the gas (which is 88.2% argon, 9.8% methane and 2% isobutane at 4 bar). The measurement of up to 159 points per track and an excellent two-track resolution guarantee a high tracking efficiency. The chamber is 4 m long with an inner diameter of 0.5 m and an outer diameter of 3.7 m. The sensitive volume of the jet chamber is divided into 24 identical sectors, each containing a plane with 159 sense wires. Cathode wire planes form the boundaries between adjacent sectors.

Z Chambers

Z-chambers, mounted around the outer mechanical support of the jet-chamber, are used to obtain a precise measurement of the z coordinate of the tracks, thereby improving the polar angle invariant mass resolution. The z-chambers are arranged to form a barrel layer around the jet chamber covering the polar angle from 44° to 136° degrees and 94% of the azimuthal angle.

3.2.3 Calorimeters

The calorimeters are made of high density material, and they are designed to stop most of the particles originating from the electron-positron interaction. When electrons, photons or hadrons stop in the material of the calorimeters, they give rise to showers. The energy of the incoming particle is measured from the properties of these showers.

Electromagnetic Calorimeters

The electromagnetic calorimeter detects and measures the energies and positions of electrons, positrons, and photons ranging from tens of MeV to 100 GeV. It provides π^0-photon discriminations and, in conjunction with the central tracking system, electron-hadron discrimination. It is a total absorption calorimeter and is mounted between the coil and the iron yoke of the magnet. The electromagnetic calorimeters are made of lead-glass blocks, and they cover nearly all angles from the beam direction. Most particles produced in the electron-positron collisions are absorbed in the electromagnetic calorimeters.

Hadron Calorimeters

The hadron calorimeter lies outside the electromagnetic calorimeter. It is largely made of iron, and it catches particles which have penetrated through the electromagnetic calorimeter.
The hadron calorimeter measures the energy of hadrons emerging from the electromagnetic calorimeter and assists in the identification of muons. The iron of the magnet return yoke provides 4 or more interaction lengths of absorber over a solid angle of 97% of 4π. The yoke is segmented into layers, with planes of detectors between each layer, and forms a cylindrical sampling calorimeter about one meter thick.

3.2.4 Muon System

This detector identifies muons, in particular in the presence of a background of hadrons. The muon detector is constructed as a barrel and two endcaps and covers the iron yoke almost completely. Of the full solid angle, 93% is covered by at least one detection layer.

3.2.5 Forward Detectors

The forward detector is used for luminosity measurement by using small angle and Bhabha scattering, and to tag electrons from $\gamma\gamma$ interaction. It consists of two detectors:

- The forward detector (FD) - consists of drift chambers that are used to reconstruct tracks from electrons that do not shower in the beam pipe, and proportional chambers to provide measurement of the shower position in the θ and ϕ. The calorimeter is designed to measure the ϕ angle of the shower position and to give shower development information. The small electromagnetic calorimeter (gamma catcher) is designed to cover the gap in calorimetric acceptance between the forward detector and the electromagnetic end-cap calorimeter. Its main purpose is to veto background events to processes such as $e^+e^- \rightarrow Z^0\gamma$, with $Z^0 \rightarrow \nu\nu$.

- The silicon tungsten detector (SW) - a newer forward detector that had been in use since 1993. It is composed of two calorimeters that are finally segmented both radially and longitudinally so that they can achieve very good position and energy resolutions. The calorimeters are located at $\pm 239\ cm$ in z from the e^+e^- interaction point. At the front of each calorimeter, there are layers of bare silicon and tungsten. The front layers are used for determining the incidence angle of electrons and photons (hence the luminosity) and the back ones (where the showers are the widest) measure the energy.

3.2.6 Trigger

The trigger system initiates the readout of the detectors. The OPAL trigger contains a high degree of redundancy, so that the efficiency for accepting multi-hadronic events is greater than 99%.
The trigger should accept real e^+e^- events, and suppress background events like cosmic radiation, reaction with atoms in the beam pipe etc. It reduces the 90 kHz bunch crossing rate, to a rate less than 10 Hz, which can be handled by the data acquisition system.

The following sub-detectors provide the trigger signals:

- The track trigger - using input from the vertex detector and the jet chamber.

- The energy trigger - using the energy deposit in the electromagnetic calorimeter.

- The muon trigger - from the muon chamber.

- The time-of-flight trigger.

- The two luminosity triggers - from the forward detectors.

Each sub-detector provides two categories of signal: 'stand alone' signals such as multiplicity counts or energy sums over the entire detector, and signals from a 6×24 binning in θ and ϕ (respectively). The trigger processor makes its decision by forming correlations in space between binned sub-detector signals, and using these correlations together with the stand-alone signals.

3.2.7 Track Reconstruction

By definition, any CJ segment found is a track. A list of hits for each track is built and independent track fits are done in $r - \phi$ and in s-z (s is the $r - \phi$ path integral from the point of closest approach of the track to the origin). The $r - \phi$ fit uses the Billoir method [8] which adds in the multiple Coulomb scattering errors. A systematic measurement error term is also added to the covariance matrix. For the s-z fit, it is assumed that there is no error in s relative to the intrinsic error in z. The multiple scattering error estimate and a systematic error term are added after the fit.

A CJ track is a necessary requirement for all tracks. The track merging attempts to add CV axial and stereo segments and CZ segments to each CJ track. The order in which the associations are made can be changed by the user, but the default is to first match CJ with CV axial segments, then with CZ segments, and finally with CV stereo segments. After each stage of the merging the CJ track parameters are updated in view of any matches, and the next stage of the merging uses these modified parameters. After all three

Detector type	Sub-detector	Function
Semiconductor	SI	Silicon micro-vertex detector, search for impact in the micro-vertex detector
	SW	Silicon-Tungsten Luminometer, tracking and calorimetry in the forward region
Multi-wire proportional chamber	PE	Electromagnetic presampler
	HP	Hadron calorimeter, pole-tip
	FD	Forward detector, tracking and calorimetry in the forward region
Drift chamber	CV	Central vertex chamber, tracking in the central detector
	CJ	Central jet chamber, tracking in the central detector
	CZ	Z chamber, tracking in the central detector
	MB	Tracking in the muon barrel
Streamer tubes	PB	Electromagnetic presampler
	HB	Hadron calorimetry, processing of the barrel
	ME	Muon end-cap
Scintillation counter	TOF	Time of flight detector
	FD	Fine luminosity monitor
	GC	Gamma catcher
Lead glass detector	EB	Electromagnetic calorimeter (barrel)
	EE	Electromagnetic calorimeter (end-cap)

Table 3.1: OPAL sub detectors by operating principal.

types of merging have been considered, the lists of associated CJ, CV axial, CV stereo, and CZ segments are used to construct lists of hits for the final track fits.

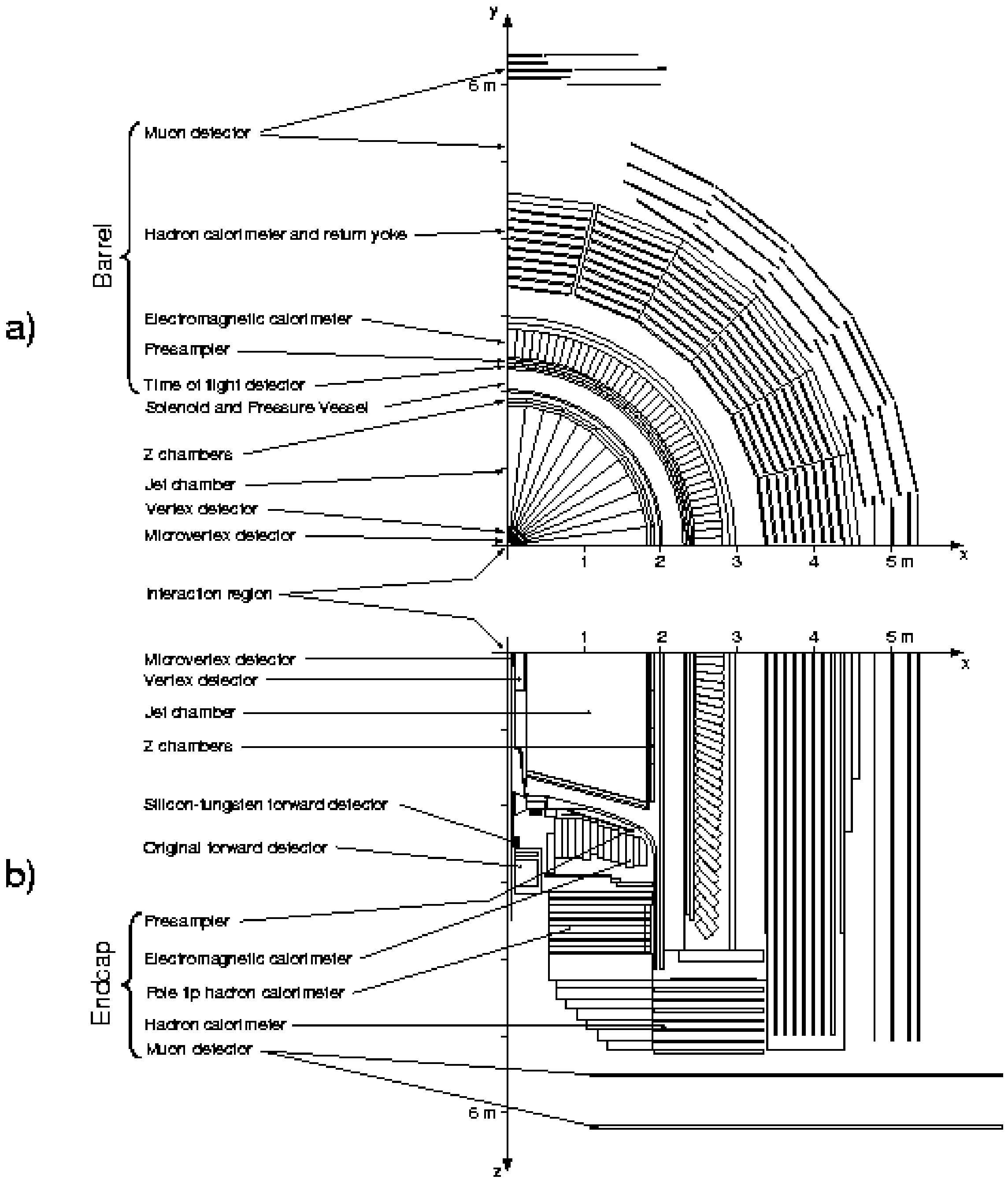

Figure 3.3: Cut through the OPAL detector. (a) perpendicular and (b) parallel to the beam axis.

Chapter 4

Tools for Selection and Reconstruction

In each event, tracks and electromagnetic clusters not associated to a track are combined into jets, using the JADE algorithm (see section 5.2). The primary vertex of the event was reconstructed using the tracks in the event and the knowledge of the position and spread of the e^+e^- collision point.

4.1 The Data Sample

The data used for this analysis were collected from e^+e^- collisions at LEP during 1990-1995 (LEP1), with a center-of-mass energy around the peak of the Z^0 resonance.

4.1.1 Multi-Hadronic Event Selection

There are several standard event selection used in OPAL, of which three are relevant to these analyses - the 'Gold-Plated' multi-hadronic event selection, the 'Tokyo' multi-hadronic event selection and the BT event selection [9].

Gold-Plated Multi-hadronic Event Selection

The Gold-Plated Multi-Hadronic event selection (GPMH) is an online event classification. Electromagnetic energy clusters in the barrel are required to have a 100 MeV block and at least one nearest neighbour with 50 MeV. In the endcap the thresholds are 200 MeV for the initiating block and 100 MeV for the nearest neighbour.

A GPMH event is required to satisfy the following criteria:

- At least 6 electromagnetic clusters, with the sum of their energies greater than 8 GeV.
- The sum of the cluster energies in the hemisphere opposite to the highest energy cluster is greater than 2 GeV.
- The event is required to pass the halo-muon rejection cut.
- The event contains at least three hits in the time of flight counters.

Tokyo Multi-hadronic Event Selection

The Tokyo Multi-hadronic event selection (TKMH) is the standard event selection used for the study of hadronic cross sections. The TKMH is made offline, using cuts that are designed to reject:

- Z^0 decays into leptons, by setting a lower limit on the number of clusters and tracks.
- Cosmic rays background by requiring a vertex for tracks.
- Two photon, beam-gas and beam-wall events, by setting a lower limit on the ratio between the energy deposited in the electromagnetic calorimeters and the center of mass energy, and by requiring a low energy imbalance along the beam direction.

This selection gives a very high hadronic selection efficiency and a background of less than 0.1%.

4029364 hadronic events were selected.

BT Selection

The BT is an additional selection to the TKMH. It requires cuts on the track multiplicity and the angle of the thrust axis.
It is designed to eliminate $\tau^+\tau^-$ events and was estimated to have an efficiency of $97 \pm 1\%$.

4.1.2 Charged B Events

The measured fraction R_b of $Z^0 \to b\bar{b}$ in hadronic Z^0 is (see [1])

$$R_b = \frac{Z^0 \to b\bar{b}}{Z^0 \to q\bar{q}} = 0.21646 \pm 0.00065 \tag{4.1}$$

furthermore, the b-hadron fraction to form charged B meson is:

$$b \to B^+ = 0.401 \pm 0.011 \tag{4.2}$$

Using the numbers above, the estimation for the number of charged B mesons in the sample is 699501 ± 88800.

4.2 Jet Finding

The underlying structure of multi-jet hadronic events can be found by using different algorithms. We used the JADE algorithm with the E0 recombination scheme [10]:
For all pairs of particles k and l of an event, the scaled invariant mass squared $y_{kl} = \frac{M_{kl}^2}{E_{vis}^2}$ is calculated, where E_{vis} is the total visible energy of an event.
The two particles with the smallest values of y_{kl} are replaced by a pseudoparticle of four-momentum $(p_k + p_l)$. This procedure is repeated until all y_{kl} exceed a certain threshold value y_{cut}, and the resulting number is called

the jet-multiplicity of the event. The expression used for calculating the invariant squared mass is:

$$M_{kl}^2 = 2 \cdot E_k \cdot E_l \cdot (1 - cos\theta_{kl}) \tag{4.3}$$

E_k is the energy of (pseudo)particle k.
E_l is the energy of (pseudo)particle l.
θ_{kl} is the angle between the k and the l (pseudo)particles.

This choice of M_{kl} provides the closest agreement between cluster and parton-multiplicities at comparable values of y_{cut} (the experimental cutoff in the cluster algorithm) and y_{min} (the QCD cutoff parameter for the massless partons in the $\mathcal{O}(\alpha_s^2)$ model). With this algorithm jets are defined by $y_{cut} = 0.04$, which corresponds to a minimum invariant pairmass of 6.8 GeV/c^2 and is a reasonable choice for the definitions of jets.
At this value of y_{cut} the rates of 5-jet events are less than 0.1%.

4.3 Monte-Carlo

An important tool for the data analyses in high energy physics is the simulation of physics events called Monte-Carlo.
Monte Carlo events are used, for example, for estimating the selection efficiencies and backgrounds.
Monte Carlo event generation consists of two parts:

- The event generator which generates production and decay chains of particles. The common generator used for $e^+e^- \rightarrow hadrons$ events is the JETSET [11].

- The detector simulation which simulates the readout of the detector response to the generated ‘particles ’ . This simulation program contains a detailed description of the detector. For OPAL the GOPAL [12] package was used.

4.3.1 The Event Generator - JETSET

The perfect event generator does not exist. A perfect generator can be designed only once all is known - and by that being useless. Programs being used are those with a reasonable agreement with existing theoretical and experimental results, and provide sensible extrapolations to higher energies. For this reason event generators are being constantly modified and improved. An e^+e^- event generation process must consider the following components, which are illustrated in figure 4.1:

- The hard scattering matrix elements: these define the process under study. e^+ and e^- annihilate to a Z^0 or a photon, which decay to a pair of quarks. The mode must consider initial state radiation. This process is calculable within the Standard Model to a very high accuracy.

- Final state radiation: partons (quarks and gluons) in the final state may radiate. At high energies this perturbative radiation is the dominant mechanism for building up the structure of jets. This phase can be calculated using perturbation theory in QCD, as long as the strong coupling constant α_s is small. In leading order the α_s dependence on the momentum transfer q^2 is:

  $$\alpha_s(q^2) = \frac{4\pi}{(11 - \frac{2}{3}N_f)ln(\frac{q^2}{\Lambda^2_{QCD}})} \tag{4.4}$$

  where N_f is the number of active quark flavor (here 5, no top production at LEP), and Λ_{QCD} is the QCD scaling parameter. In the limit $q^2 \rightarrow \infty$, $\alpha_s \rightarrow 0$. As the momentum transfer decreases α_s increases, and the perturbation theory does not converge. A cutoff parameter is therefore implemented in JETSET at which the parton shower stops.

- Fragmentation: partons are not directly observable. As q^2 decreases α_s increases and it's not possible to use perturbation theory anymore. QCD phenomenological models are being used. JETSET uses the so-called "string model". In this model, as the distance between two quarks increases, the colored "string" connecting them has enough energy to form another $q\bar{q}$ pair in a hadronization process that is described using many parameters. Heavy quark fragmentation in parametrized by the Peterson fragmentation function [13].

- Decays: the hadrons decay to particles visible in the detector. Decay rates of previous measurements are used.

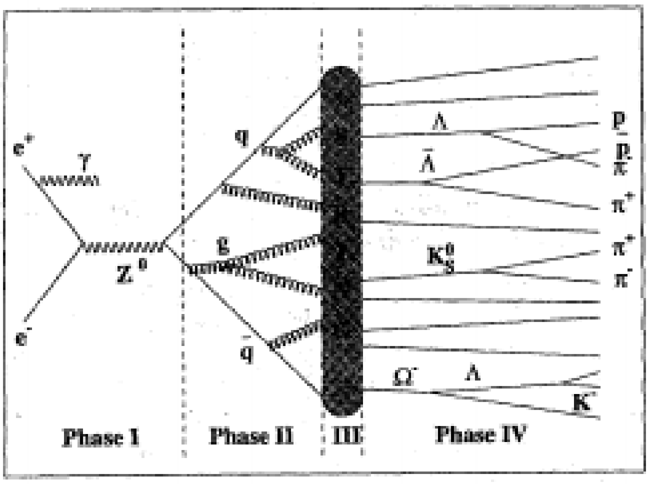

Figure 4.1: Phases of the process $e^+e^- \rightarrow$ hadrons.

4.3.2 GOPAL - The Detector Simulation

The GOPAL detector simulation is using the GEANT package to simulate the interaction of particles with the detector material [12]. GEANT provides a framework for the definition of the detector geometry and the simulation of the interaction of particles traversing the geometry. The program traces each particle, starting from the kinematics and generates hits when it traverses the sensitive detectors. The particles are allowed to loose their energy, generate other particles, decay or vanish as they interact with the detector material. At the end of the simulation of an event, the hits generated during the particle tracing are digitized simulating the response of the detector.

4.3.3 Monte Carlo Event Samples

Monte Carlo simulated event samples of hadronic Z^0 events are used to check the selection procedure.

These simulated event samples include:

- The decay modes that are searched for - 'signal Monte Carlo' . Figure 4.2 shows a Monte Carlo simulated $B^- \rightarrow \pi^-\pi^-K^+$ projected on the plane perpendicular to the beam.
- Generic $Z^0 \rightarrow q\bar{q}$ decays, where q is any of the five quarks - u,d,s,c,b.
- $Z^0 \rightarrow c\bar{c}$ decay sample, to verify that there is no background domination from this process
- $Z^0 \rightarrow b\bar{b}$ decay sample, to verify that there are no other specific decays dominating the background.

4.4 *dE/dx* - Energy Loss

A particle passing through matter interacts with electrons and with nuclei, possibly also with the medium as a whole (Cerenkov radiation, coherent bremsstrahlung). A light projectile colliding with a heavy target particle will be deflected (multiple scattering), but will loose little energy unless the collision is inelastic. A heavy projectile colliding with a light target will loose energy without being appreciably deflected.
The average energy loss of a hadron is mainly due to strong interactions, which eventually even destroy the particle (calorimeters). Nevertheless, electromagnetic energy loss of hadrons is important, because the mean free path for strong interactions (collision length) is large.
Except when the projectile is highly relativistic, ionization is the main electromagnetic contribution to the energy loss for charged particles. The mean energy loss (the stopping power) due to ionization is given by the Bethe-Bloch

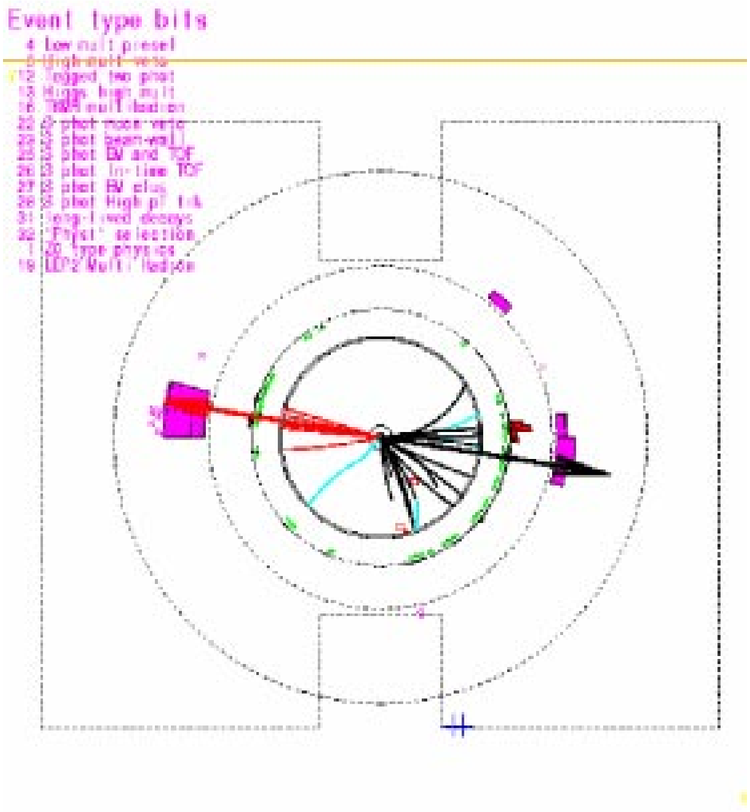

Figure 4.2: Display of an event simulation from the process $B^- \rightarrow \pi^-\pi^-K^+$. The Z^0 splits into two primary $b\bar{b}$ quarks that make hadronization into different particles that further decay.

formula, and depends on the particle velocity β and the charge number Q:

$$\frac{dE}{dx} \propto \frac{QZ}{\beta^2}[\frac{1}{2}ln\frac{2m_e(\beta\gamma)^2T_{max}}{I^2} - \beta^2 - \frac{\delta(\beta\gamma)}{2}] \tag{4.5}$$

Where $\gamma = (1-\beta)^{-1/2}$, Z is the atomic number of the medium, m_e is the electron mass, T_{max} is the maximum kinetic energy which can be imparted to a free electron in a single collision. I is the minimum excitation energy, $\delta(\beta\gamma)$ is the density effect correction function.
The Bethe-Bloch equation is a universal function of $\beta\gamma = \frac{momentum}{mass}$ for all particle species.

Measurements of energy loss can be used to identify particles if a simultaneous measurement of the momentum is available.

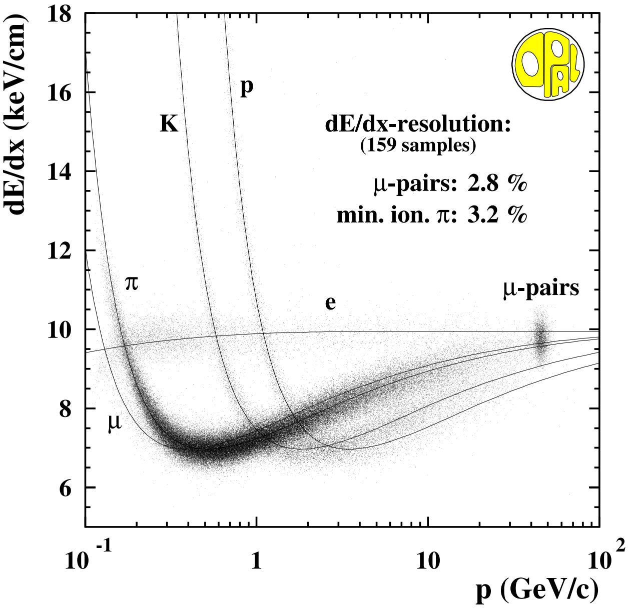

Figure 4.3: dE/dx measurements in multihadron events.

Figure 4.3 shows the measured dE/dx versus the track momentum for hadron tracks and muon-pairs together with the expected functional form.
A track is given a dE/dx weight, which is the signed χ^2 probability of it being consistent with a certain particle species. The sign of the weight corresponds to the sign of the difference $dE/dx_{measured} - dE/dx_{expected}$, where the $dE/dx_{expected}$ is the expected dE/dx according to the measured momentum of the particle species in question.
Therefore the pure χ^2 probability, $P(\chi^2)$, is given by

$$P(\chi^2) = abs(weight) \tag{4.6}$$

.
The distribution of the dE/dx weight of a track to result from a certain particle is one of the most important means for selecting and rejecting tracks. For example - when looking for kaons, one would reject tracks that according to their dE/dx weights are most likely to be pions, while keeping tracks that according to their weights seem to be kaons.

4.5 Artificial Neural Network

In the search for the specific decays we are interested in, the B meson candidate is reconstructed from combinations of tracks that passed a certain optimized selection. A selection like this can be performed by selecting events that passed some discriminating parameter cuts, in order to achieve a good separation between signal and background events. However, even when having the right signal track combination, using hard cuts on certain variables may lead to the loss of a signal combination due to one cut failure. In order to avoid cases like this, we would be interested in a selection based on a method which looks at the overall event characteristics, rather than on individual variables only. Moreover, the method of placing hard cuts on different variables ignores correlations between these variables, while using these correlations may improve the selection. An Artificial Neural Network (ANN) is a classification technique having these advantages.
ANNs are very useful in high energy physics, because they are especially powerful for classification of problems which are tolerant of some imprecision, which have lots of training data available, but to which hard and fast rules cannot easily be applied. An Artificial Neural Network is a network of many simple processors (units), each possibly having a small amount of local memory. The units are connected by communication channels, which usually carry numeric data.

4.5.1 The ANN Procedures Used for the Analyses

Each of the circles in figure 4.4 is called a unit (or neuron) containing an input-output transfer function, chosen from a variety of transfer functions;

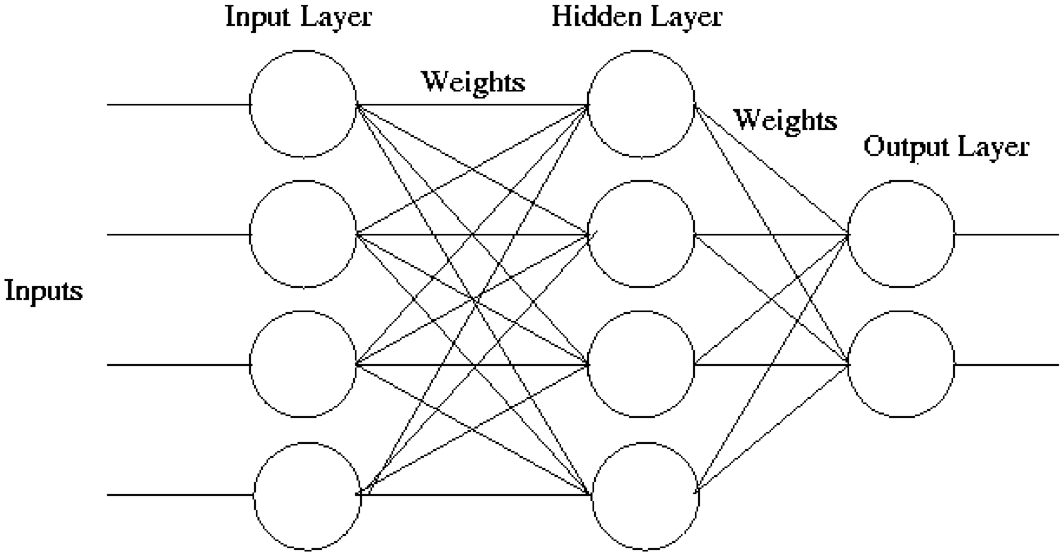

Figure 4.4: General schematic of a feed-forward neural network.

among the more popular ones are the logistic-sigmoid and the tangent-sigmoid functions. Both the input and the output are scalar-valued. The three column-arrangements of the units are called layers. From left to right in Figure 4.4 they are labeled the input, hidden, and output layers. For the event selection a 3-layer network is used, but in general any number of layers can be used.

Layers are connected to each other by a system of weights, which multiplicatively scale the values traversing the links.

A feed forward ANN based on the JETNET3 package [14] and trained with the back propagation of error algorithm [15] is used, with one hidden layer and two hidden units per input parameter, which is the most simple ANN architecture that already provides a non-linear response function.

There are 2 sets of weights: one connecting the input to the hidden layer, and the other from the hidden to the output layer. For the feed-forward ANN the following form of feature functions in terms of the kinematic variables is chosen:

$$F_i(\vec{x}) = g[\frac{1}{T}\sum_j w_{ij}(\frac{1}{T}\sum_k w_{jk}x_k + \theta_j) + \theta_i] \tag{4.7}$$

$\vec{x}$ is the set of input variables (patterns) $\vec{x} = (x_1, x_2, x_3, ...x_n)$ where n is the number of input variables.

The weights w_{ij} and w_{jk} are parameters to be fitted to the data distribution (via a training process), the θ_i term is a threshold corresponding to the membrane potential in a biological neuron. $g(\vec{x})$ is a non-linear activation function (or 'transfer' function). g typically is a sigmoid-shaped function. For the ANN used for the search the activation function is of the form:

$$g(a) = \frac{1}{2}[1 + tanh(a)] = (1 + e^{-2a})^{-1} \tag{4.8}$$

The feature functions are used to categorize the set of input patterns ($\vec{x}$). The input variables are fed into an input layer (receptors) and the output nodes represent the feature. T is the ‘temperature’ . A low temperature corresponds to a very steep sigmoid and a high temperature corresponds to an approximately constant g function. The input layer in figure 4.4 corresponds to the discriminating variables x_k and the output layer to the feature function F_i. The hidden layer enables non-linear modeling of the data, connecting the input layer and the output layer.

‘Backpropagation of error’ means that the weights w_{ij} and w_{jk} are determined by minimizing an error measure of the fit. For architectures with non-linear nodes, no exact procedure exists for minimizing the error, and one has to rely on iterative methods [16].

The ‘back-propagation’ training of the ANN must have a “teacher” . The training should be done by using a data sample with a known output, in order for the ANN to learn how to classify the problem.

Once the weights have been fitted to the data in this way (using labelled data), the network should be able to classify data it has never seen before. The ability of the network to correctly model such unlabelled data is called 'generalization performance'.

The application of the ANN is done in the following way:

- A Monte Carlo dataset is created, containing two classes of events - signal events and background events. Several candidate separation variables, which could be used as an input to the ANN, are chosen.
- The training of the ANN is based on the various available inputs, which are chosen to have good separation power between signal and background, and which are also least correlated ones. The performance

of various network configurations and sets of input variables are compared, and an optimal ANN (i.e one that gives best event classification) is trained. All input distributions (for background and signal) are given to the ANN after transformations to the 0-1 range (for example - tanh).

- From the training process a classification subroutine is created. This subroutine calculates the ANN output given the appropriate inputs. This can be used in a stand-alone program, as part of further selection. The output value varies between 0 to 1, where 1 corresponds to signal-like event and 0 corresponds to a background-like event.

Chapter 5

K_s^0 identification

The OPAL experiment already had a good routine for reconstructing K_s^0 candidates. However, by applying an ANN for the K_s^0 selection the performance of this routine has improved [17].
The two main decay modes of K_s^0 are:

$$K_s^0 \to \pi^+\pi^-(68.61 \pm 0.28)\% \tag{5.1}$$

$$K_s^0 \to \pi^0\pi^0(31.39 \pm 0.28)\% \tag{5.2}$$

Neutral pions don't leave tracks while passing through the detector and for this reason the second decay mode of the K_s^0 mentioned above can not be used to reconstruct K_s^0 candidates. As tracks are easily identified, the reconstruction of K_s^0 candidates is done by combining tracks that are assigned to opposite electrical charges, and their invariant mass is calculated under pion-pion hypothesis.

5.1 One Dimensional Pre-selection Cuts

Before using an ANN selection some pre-selection cuts based on the OPAL IDV0ID routine [18] were used (figure 5.4):

- More than 3 Z-chamber hits, or reconstructed end-point inside the jet-chamber .
- The radial distance between the intersection point and the primary vertex should be greater than 1 cm and less than 1.5 cm.

- The radius of first jet-chamber hit is less than 3 cm from the secondary vertex if the secondary vertex was reconstructed inside the jet-chamber volume.
- The radial distance from track to the beam axis at the point of closest approach is greater than 3 mm, if secondary vertex is not reconstructed inside the jet-chamber.

5.2 ANN Performance

The ANN is given the following variables as input parameters:

- p_{xy}, the momentum in the plane perpendicular to the beam axis for each of the tracks.
- The number of CJ (jet-chamber) hits for each of the tracks.
- The larger radius of the two intersection points.
- The difference between the two tracks along the beam axis at their intersection point.
- The angle in the plane perpendicular to the beam axis, between the line that connects the e^+e^- interaction point with the inner intersection of the two tracks and the K_s^0 momentum vector.

Figure 5.1 shows the distribution of the input variables for the signal and background two-track combinations. The Monte Carlo used for background is generic $Z^0 \to q\bar{q}$. Due to large separation between signal and background in the last distribution, candidates are chosen only if this angle is smaller than $5°$. This cut has a negligible effect on the efficiency, but reduces the sample size dramatically. Figure 5.2 shows the output of the neural network for signal and background two-track combinations.

The product of the purity of the selected sample and the relative efficiency as a function of the NN output cut value is shown in figure 5.3, where the definition of relative efficiency is with respect to $NN > 0$ (no cut). The absolute efficiency of this state ($NN > 0$), defined as the ratio of true K_s^0 that survived the selection criteria to the number of K_s^0 in the sample, is found to be 31%. An optimization of the selection according to the product of purity times efficiency leads to a cut at $NN > 0.4$.

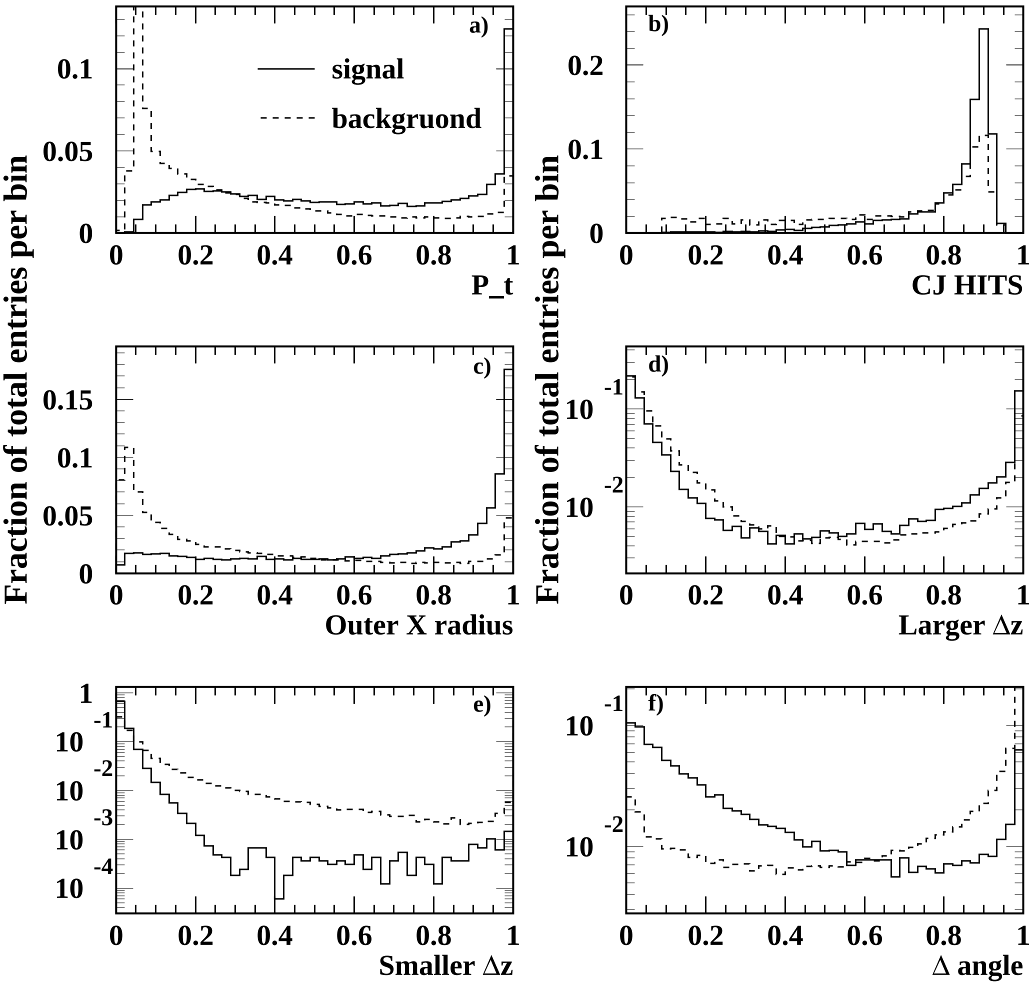

Figure 5.1: Input variable distributions for signal (solid) and background (dashed) events. All variables are plotted after a transformation to the 0-1 interval.

5.3 Systematic Uncertainties

The systematic uncertainties are estimated by applying the selection to signal candidates and background candidates from the data. Signal is defined as

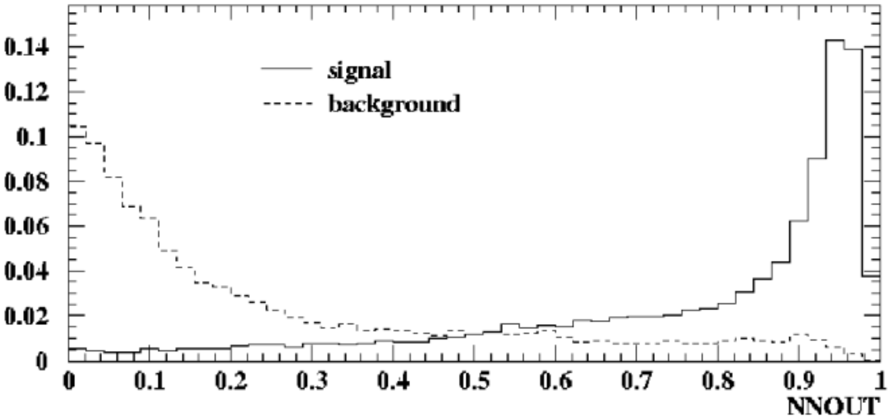

Figure 5.2: ANN output distribution for signal (solid) and background (dashed).

events that pass the IDV0ID cuts mentioned before and that are in the mass range [0.47-0.53] GeV. These events are 78% pure signal. The mass plot of these signal candidates is shown in figure 5.4. Figure 5.5 compares the input variables for background by using two-track combinations with an invariant mass of [0.3-0.4] GeV and [0.6-0.7] GeV, and figure 5.6 compares these variables for data and Monte Carlo signal events.

Figure 5.7 shows the output value for data and Monte Carlo for background events (a) and for signal events (b). In all these distributions the agreement between data and Monte Carlo is very good. The efficiency for background events to pass the $NN > 0.4$ cut is $13.6 \pm 0.1\%$ in the data and $13.9 \pm 0.1\%$ in the Monte Carlo. In the case of signal enhanced events, the efficiency for a $NN > 0.4$ cut is $96.3 \pm 0.3\%$ in the Monte Carlo and $95.8 \pm 0.3\%$ in the data. In the analysis where K_s^0 is only one of a few particles in the final state the systematic error associated with K_s^0 ANN selection is 0.7%.

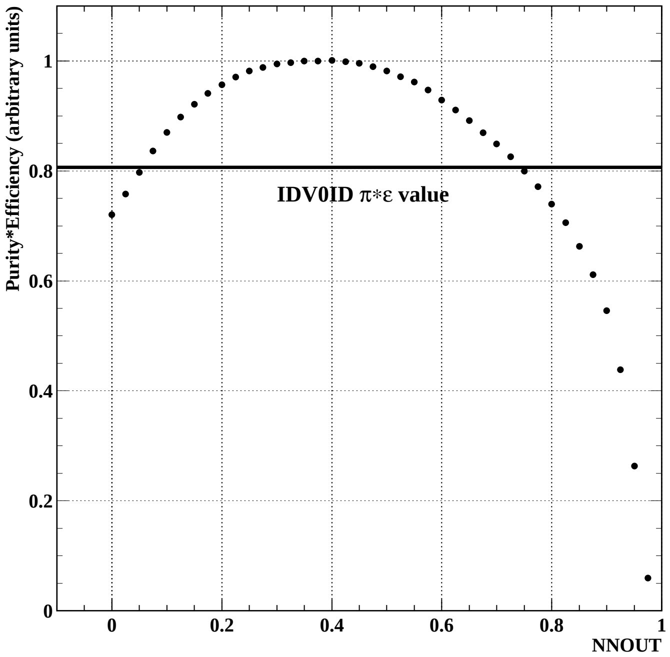

Figure 5.3: Efficiency times purity of the ANN cut. The solid line represents the value for the IDV0ID default selection.

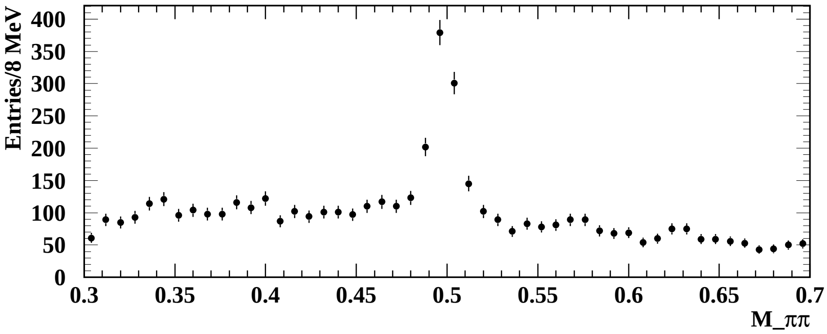

Figure 5.4: Invariant mass of candidates used as input (i.e ANN output > 0) due to the remaining cuts used by IDV0ID.

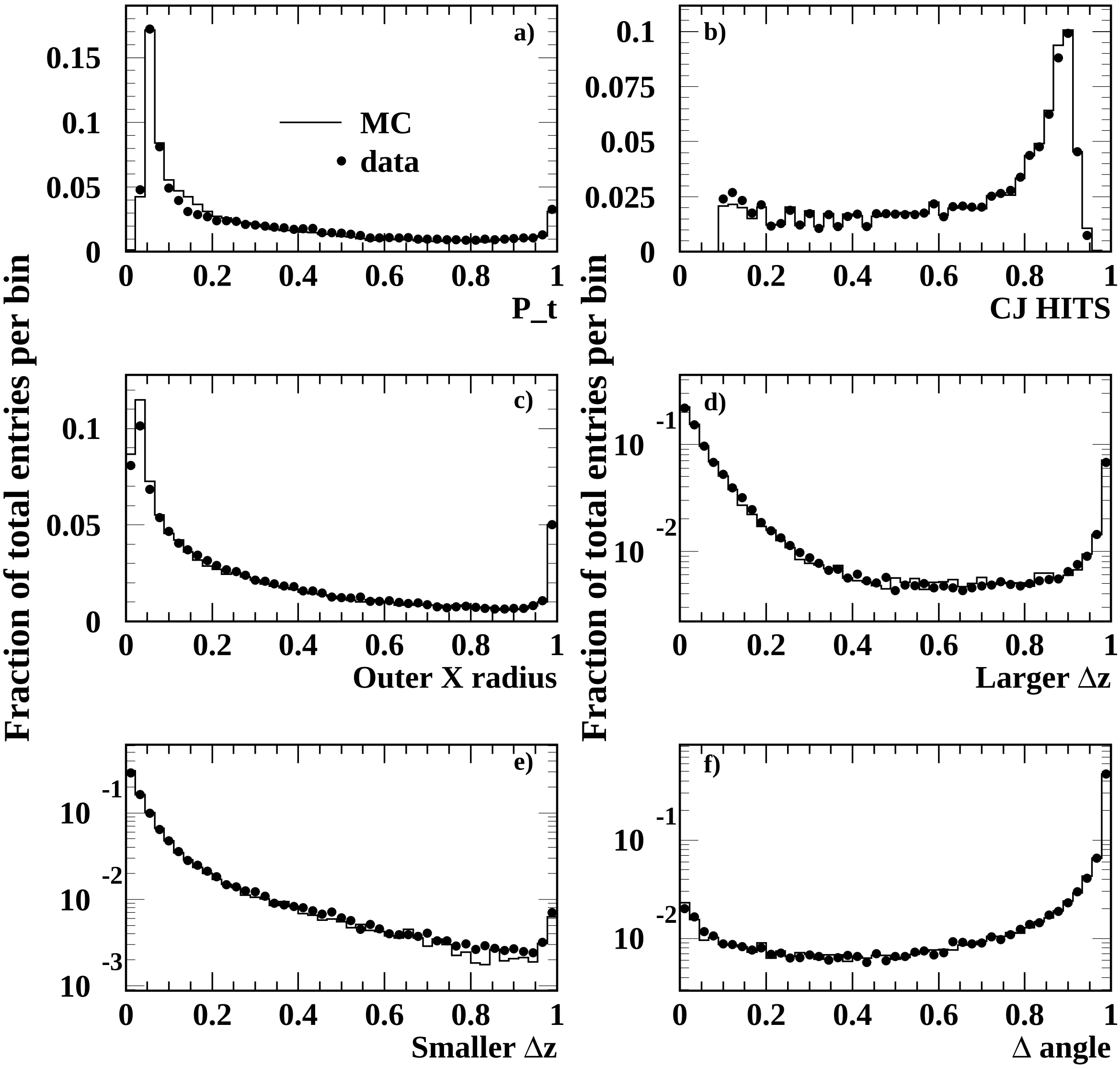

Figure 5.5: Input variable distributions for data (dots) and Monte Carlo (histogram). All two-track combinations in these plots are from the mass side-bands as defined in the text.

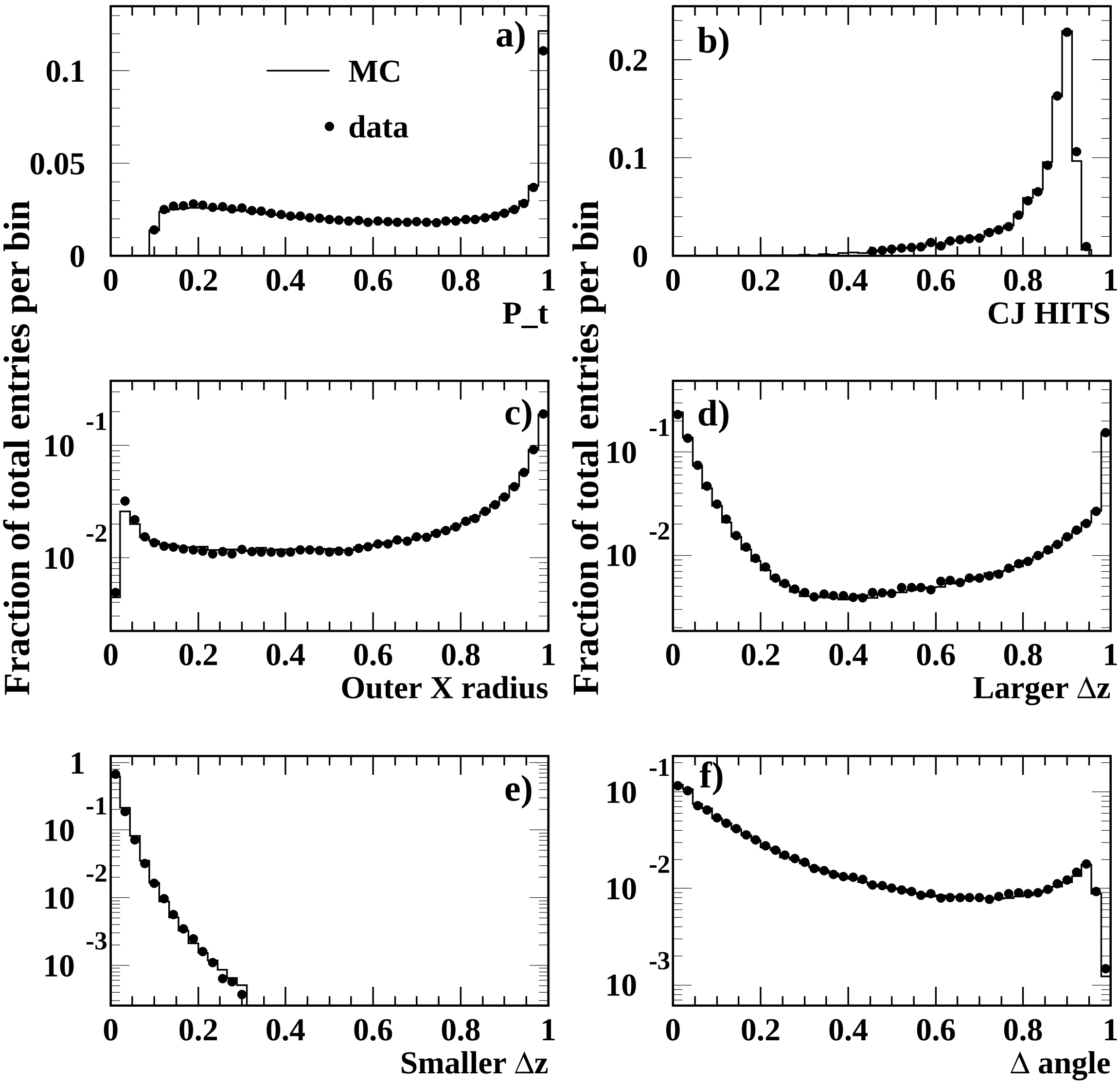

Figure 5.6: Input variable distributions for data (dots) and Monte Carlo (histogram). All two-tracks combinations in this plots are from the signal region and passed pre-selection cuts as described in the text.

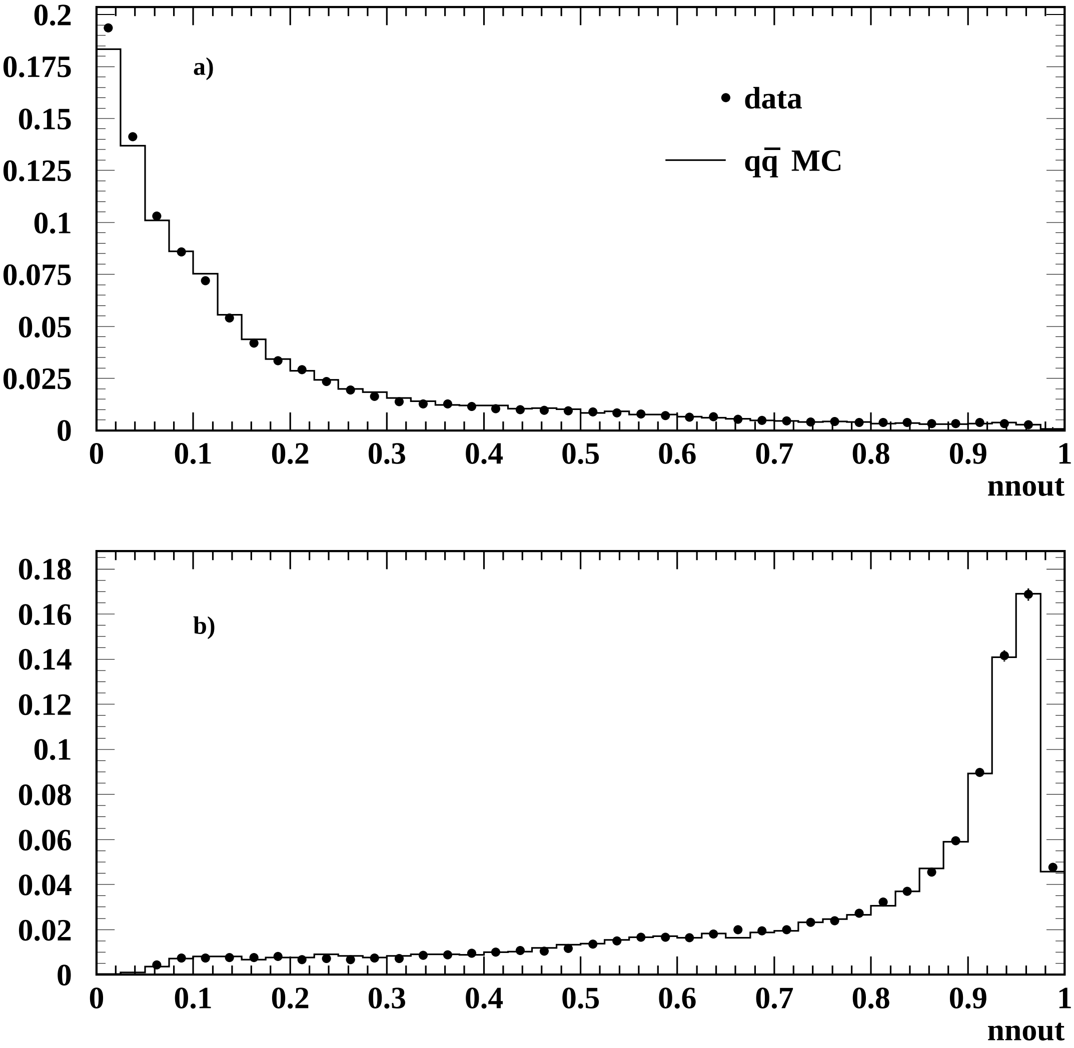

Figure 5.7: ANN output for background events (*a*) and for signal events (*b*) under the same condition as in figures 5.5 and 5.6 respectively.

Chapter 6

$B^- \longrightarrow K_s^0 K^-$ Event Selection

The search for the hadronic event sample for the decay $B^- \to K_s^0 K^-$ is done by first selecting K_s^0 candidates and then combining them with a track, that is assumed to originate from a kaon, to form a B meson candidate. All possible three track combinations are considered.
The K_s^0 candidate selection is done using the IDK0NN OPAL routine, as described in chapter 5. The track that is combined with the reconstructed K_s^0 candidate is assigned the mass of a kaon.

The requirements for the reconstruction of a B candidate are:

- All tracks (i.e, the tracks that are combined to form a K_s^0 and the track assumed to be kaon) are from the same jet.

- The kaon momentum has to be greater than 1.5 GeV/c.

- The kaon track is required to satisfy selection criteria based on the measured rate of energy loss due to ionization - the dE/dx probabilities, see chapter 4.
Tracks pass the kaon selection only if their energy loss signed-weight as kaon is below -0.1 or above 0.1 and if their energy loss signed-weight as pions is between -0.21 to 0.
These selection criteria are 90% efficient, while rejecting 33% of the background. The optimization of these cuts is done according to the maximal

value of S^2/B, S is the signal fraction passes the cut and B is the background fraction passes the cut.

• b-tagging neural network [19]: since the hadronic data sample consisted mostly of non $b\bar{b}$ events, these events are suppressed by means of a standard OPAL b-tagging algorithm, based on reconstructed displaced secondary vertices. An artificial neural network with inputs based on decay length significance, vertex multiplicity and invariant mass information is used to select vertices with a high probability of coming from a b-hadron decays.
The neural network output varies between -1g to 1. Events are accepted only if this output is greater than 0.
This cut is 50% efficient, while rejecting 84% of the background.

• Candidates are accepted if their invariant mass is in the region

$$5.1\ GeV/c^2 < M_{KK_s^0} < 5.4\ GeV/c^2, \tag{6.1}$$

which corresponds to twice the mass resolution around the nominal B^- mass.

• The final selection is based on an artificial neural network designed to select $B^- \to K^- K_s^0$ while rejecting background events, described in the following.

6.1 $B^- \to K_s^0 K^-$ ANN

The neural network uses 5 input parameters:

- $cos(\theta)$ - the angle between the vector of the $K^- K_s^0$ intersection point and the B candidate momentum.

- The transverse momentum of the kaon candidate track.

- The transverse momentum of the reconstructed K_s^0.

- The momentum (absolute value) of the kaon candidate.

- The momentum (absolute value) of the reconstructed K_s^0 candidate.

The separation between Monte Carlo simulated signal events and Monte Carlo simulated background events ($q\bar{q}$ events) can be seen in figure 6.1. All variables have a good separation power, and as can be seen in figure 6.2 there is also a good agreement between the input variable distributions from the data and from the $q\bar{q}$ Monte carlo events.

Figure 6.3 shows the output of the neural network for Monte Carlo simulated signal events and Monte Carlo simulated background events ($q\bar{q}$), and in figure 6.4 a comparison between data and Monte Carlo events is shown. Candidates with an ANN output greater than 0.9 are selected. This cut has an efficiency of 71%, while rejecting 80% of the background.

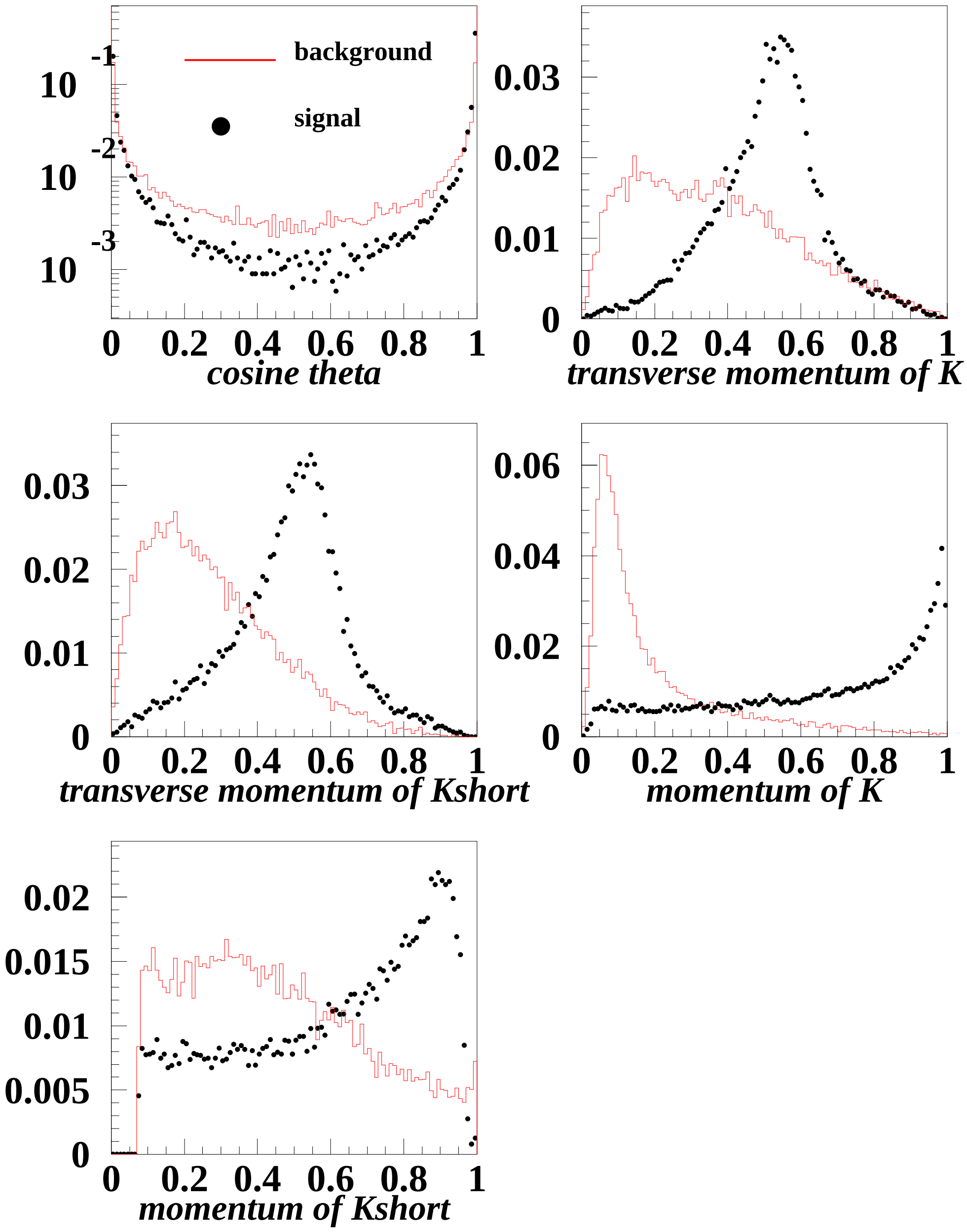

Figure 6.1: Input variables to the artificial neural network that selects $B^- \rightarrow K_s^0 K^-$ events - comparison between signal and background events; the plot of $cos\theta$ is in logarithmic scale.

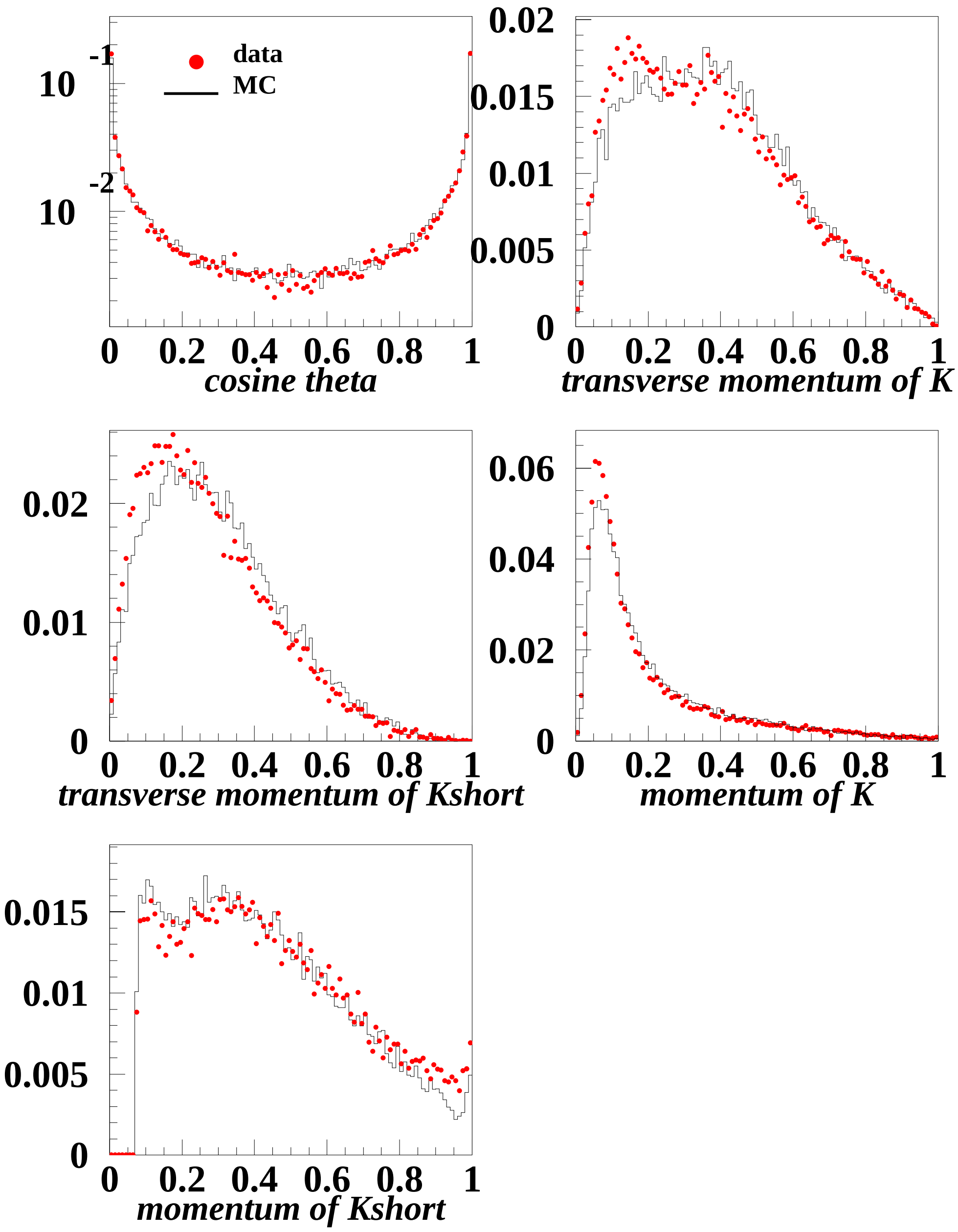

Figure 6.2: Input variables to the artificial neural network that selects $B^- \to K_s^0 K^-$ events - comparison between data and Monte Carlo events.

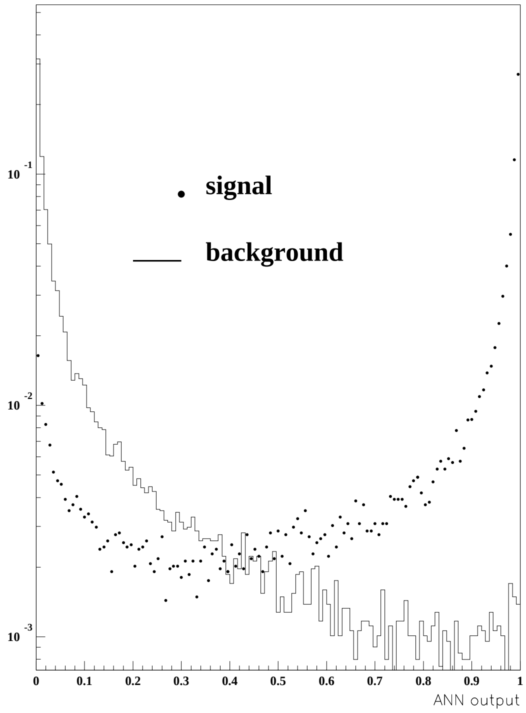

Figure 6.3: ANN output for selecting $B^- \rightarrow K_s^0 K^-$ events - comparison between signal Monte Carlo and background Monte Carlo events, plotted in logarithmic scale.

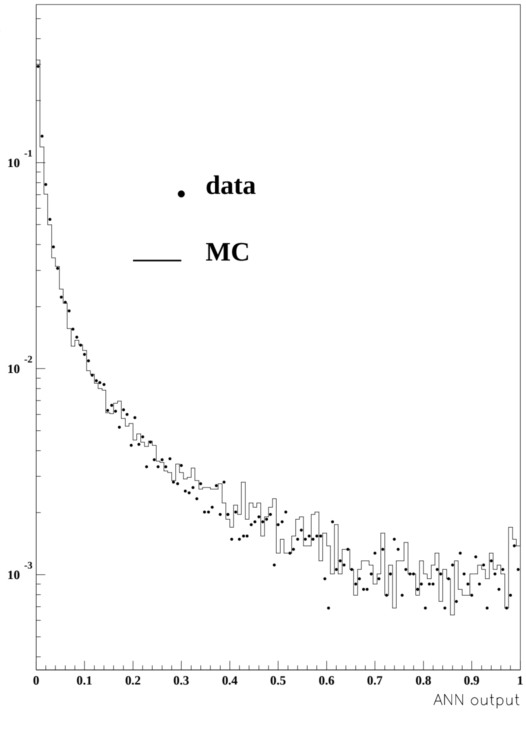

Figure 6.4: ANN output for selecting $B^- \rightarrow K_s^0 K^-$ events - comparison between data and $q\bar{q}$ Monte Carlo events, plotted with logarithmic scale.

Chapter 7

$B^- \rightarrow \pi^-\pi^-K^+$ Event Selection

The search for the event sample of the process $B^- \rightarrow \pi^-\pi^-K^+$ is done using a similar strategy as in the search for the process $B^- \rightarrow K_s^0 K^-$.
Here three tracks are combined to originate directly from one decay point. All possible combinations of three tracks are considered and B^- candidates are reconstructed from those three tracks.
Due to initial significant disagreements between Monte Carlo simulated events and the data, it is found that the search for this decay mode is very sensitive to the vertex reconstruction. As described in chapter 3.2.1, the silicon microvertex detector did not operate throughout the whole LEP run, and therefore in different periods the vertex reconstruction was done either without using the silicon microvertex detector, or with the silicon detector obtaining two or three coordinates information.
These disagreements were resolved by simulating three different Monte Carlo event samples according to the data periods. The analysis is then divided into three different samples.
The total number of multi-hadronic events in the data is 4029364. The fractions of the different samples in the data are :

⋆ 14% of the events do not have any silicon microvertex detector information.

⋆ 24% of the events have two dimensional silicon microvertex detector information.

⋆ 62% of the events have three dimensional silicon microvertex detector information.

The selection criteria are applied separately for each of the samples (data and Monte Carlo events accordingly) and finally the three samples are combined to obtain the upper limit on the branching ratio.
For each of the samples the following is required:

- All three tracks are from the same jet.

- Only combinations with the right charge signs are considered - two of the tracks are required to have the same charge, and are assigned the mass of a pion. A third track, with an opposite charge, is assumed to be the kaon.

- Tracks are required to satisfy selection criteria based on the measured rate of energy loss due to ionization (dE/dx weights):

  ⋆ dE/dx weight of a kaon candidate as a kaon between less than -0.1 or greater than 0.1.

  ⋆ dE/dx weight of a kaon candidate as a pion between -0.2 to 0.

  ⋆ dE/dx weight of a kaon candidate as a proton greater than 0.

  ⋆ dE/dx weight of a pion candidate as a kaon between 0 to 0.25.
  For the sample with the no silicon microvertex detector information the dE/dx weight cuts are 60% efficient, while rejecting 82% of the background, the same for the sample with silicon microvertex detector information for two coordinates, and for the sample with 3 coordinates silicon microvertex detector information 60.5% signal efficiency is obtained, while 82.5% of the background is rejected.

- The momentum of the kaon has to be greater than 1.5 GeV.

- The three tracks are fitted to a common vertex and the decay length, the distance from the e^+e^- interaction point to the reconstructed secondary vertex, is calculated. Candidates where the secondary vertex is in the hemisphere opposite to the candidate's jet are rejected. This criterion kept 95% of the signal and rejected 55% of the background.

- The cut on the output from the b-tagging neural network ($ANN_{output} > 0$) (see chapter 6) is 73% efficient for the signal and rejects 85% of the background.

- Candidates are accepted if their invariant mass is in the region

  $$5.1\ GeV/c^2 < M_{KK^0_s} < 5.4\ GeV/c^2, \tag{7.1}$$

  which corresponds to twice the mass resolution around the nominal B^- mass.

- The final selection is based on an artificial neural network designed to select $B^- \rightarrow \pi^-\pi^-K^+$, while rejecting background events.

7.1 $B^- \rightarrow \pi^-\pi^-K^+$ ANN

Figures 7.1 - 7.9 show comparisons of signal and background input variable distributions, $q\bar{q}$ Monte Carlo simulated events and data input variable distributions, and the ANN output distributions for each of the three samples.

The neural network used 6 input parameters:

- The averaged momentum of the pion tracks.

- The momentum of the kaon track.

- The jet multiplicity of the event.

- The minimal cosine between a pair of tracks.

- The decay length, the distance from the e^+e^- interaction point to the reconstructed secondary vertex.

- The highest momentum of the three tracks.

The ANN is trained on and applied separately to each of the three different samples.
The advantage of using silicon microvertex detector is clear from the ANN selection where the background rejection is much better when using this information. The optimization of the ANN selection (i.e the cut choices) is based on the maximal value of squared signal over background (S^2/B).
Table 7.1 summarizes the selection applied for each of the samples.
'3D SMVD' (for example) means - three dimensional silicon microvertex detector information is included.
ANN cut - is the value of the cut on the output of the ANN.
ϵ - is the efficiency for a signal event to survive the ANN cut.
BKG rejected - is the percentage of background events that is rejected by this selection.

Sample	ANN cut	ϵ	BKG rejected
no SMVD	> 0.6	81%	95.5%
2D SMVD	> 0.7	83%	95%
no SMVD	> 0.8	88%	92.2%

Table 7.1: Summary of the $B^- \rightarrow \pi^-\pi^-K^+$ ANN selections.

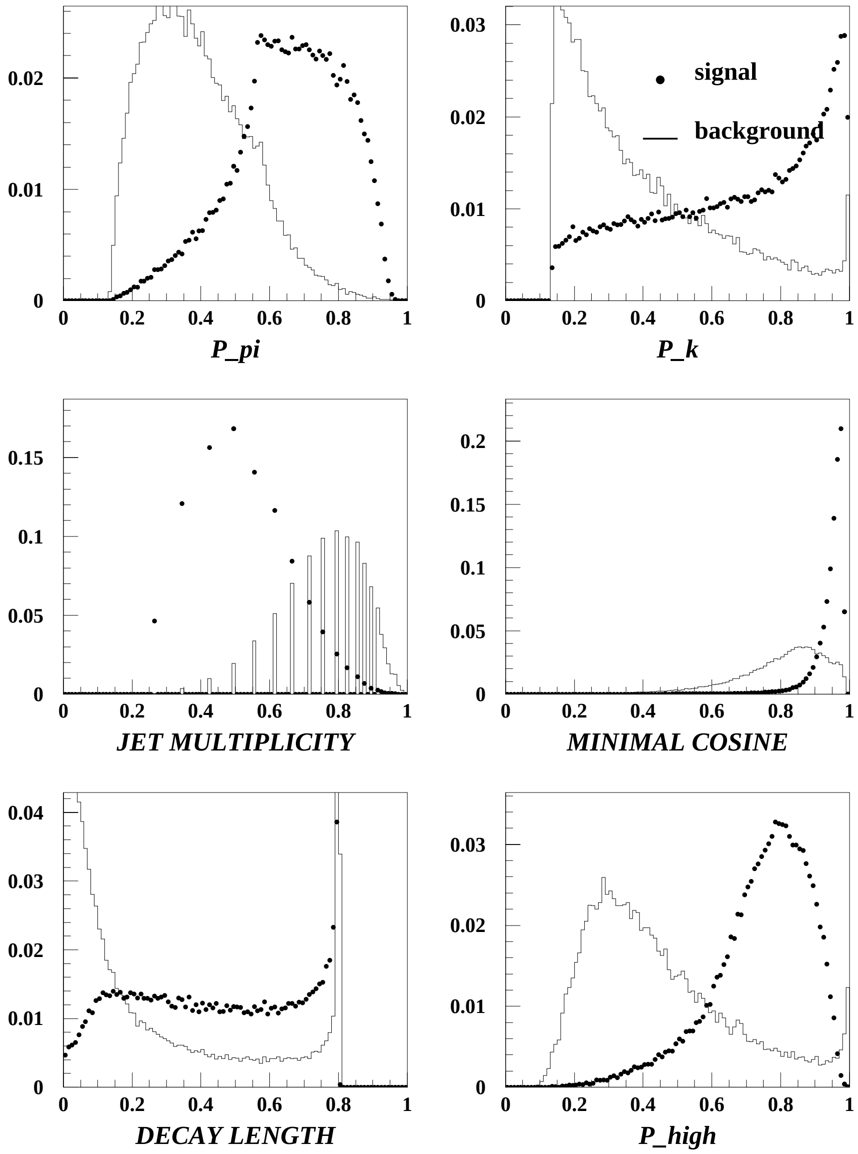

Figure 7.1: Input variables to the artificial neural network that selects $B^- \to \pi^-\pi^-K^+$ events, comparison between $q\bar{q}$ Monte Carlo events and signal Monte Carlo events simulated with three coordinates silicon microvertex detector information. All variables are normalized and are plotted after appropriate transformation to the range [0-1].

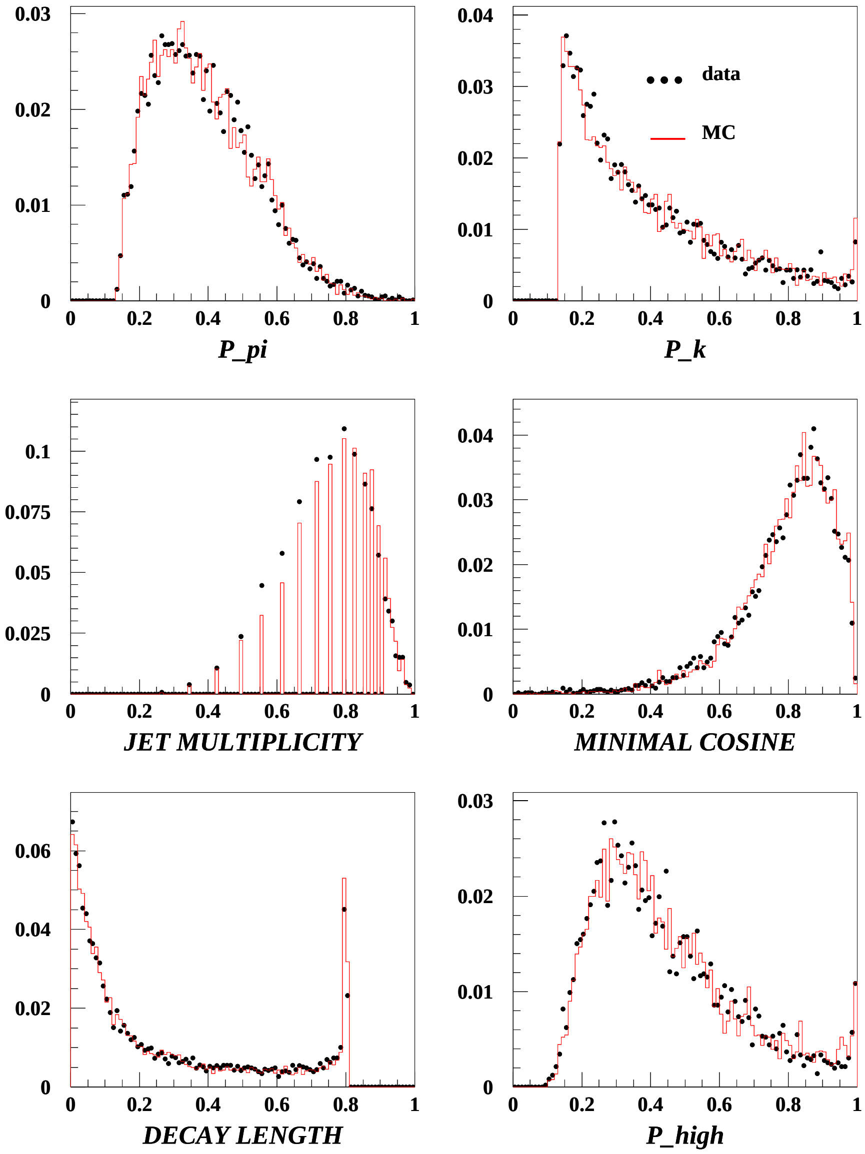

Figure 7.2: Input variables to the artificial neural network that selects $B^- \rightarrow \pi^-\pi^-K^+$ events. A comparison between $q\bar{q}$ Monte Carlo events and data that contain three coordinates silicon microvertex detector information.

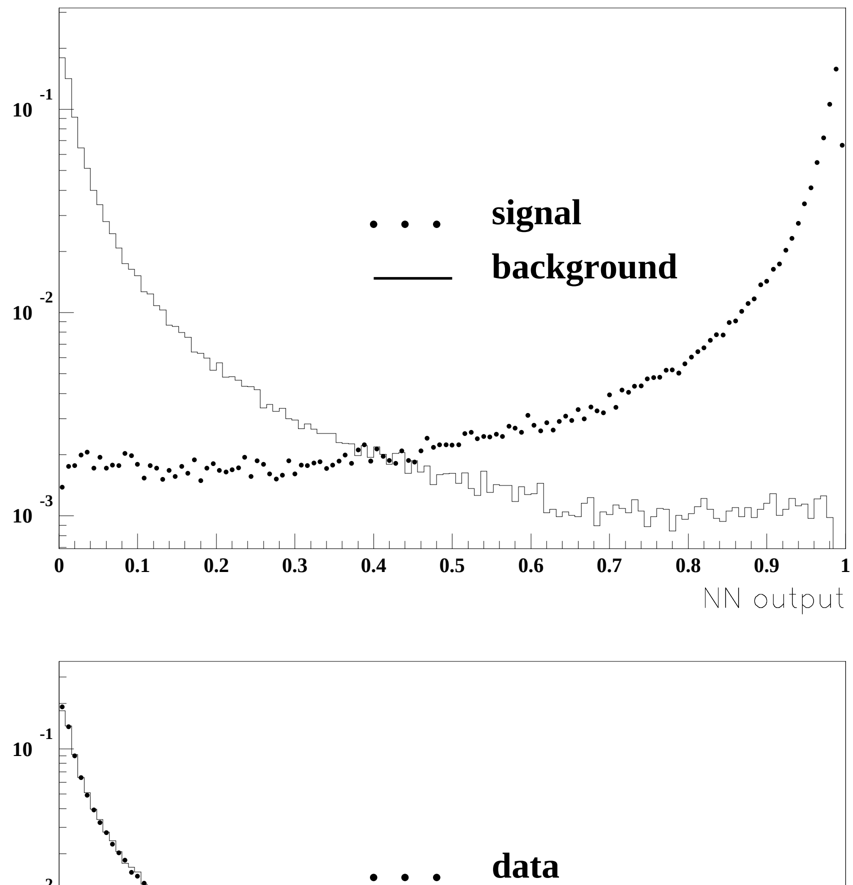

Figure 7.3: ANN output distribution for events including three coordinates silicon vertex detector information.

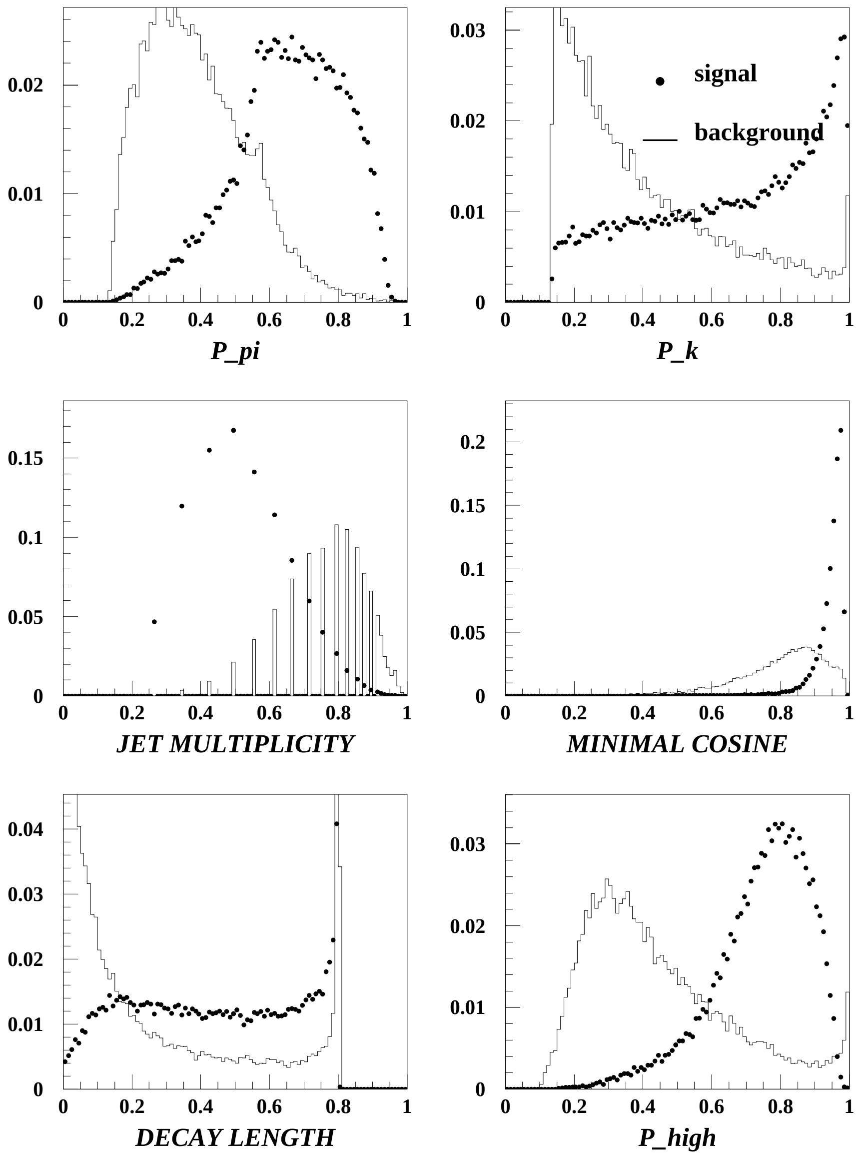

Figure 7.4: Input variables to the artificial neural network that selects $B^- \to \pi^-\pi^-K^+$ events. A comparison between $q\bar{q}$ Monte Carlo events and signal Monte Carlo events simulated with two coordinates silicon microvertex detector information.

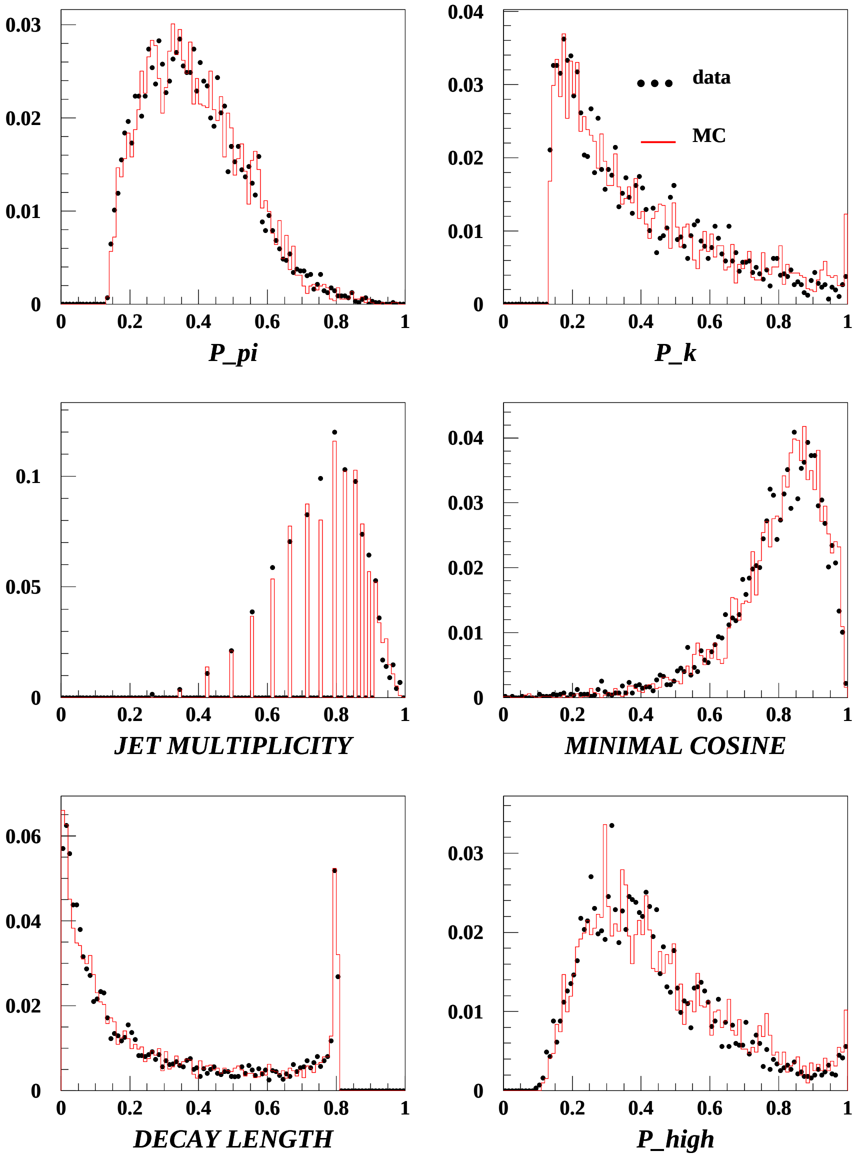

Figure 7.5: Input variables to the artificial neural network that selects $B^- \rightarrow \pi^-\pi^-K^+$ events. A comparison between $q\bar{q}$ Monte Carlo events and data that contain two coordinates silicon microvertex detector information.

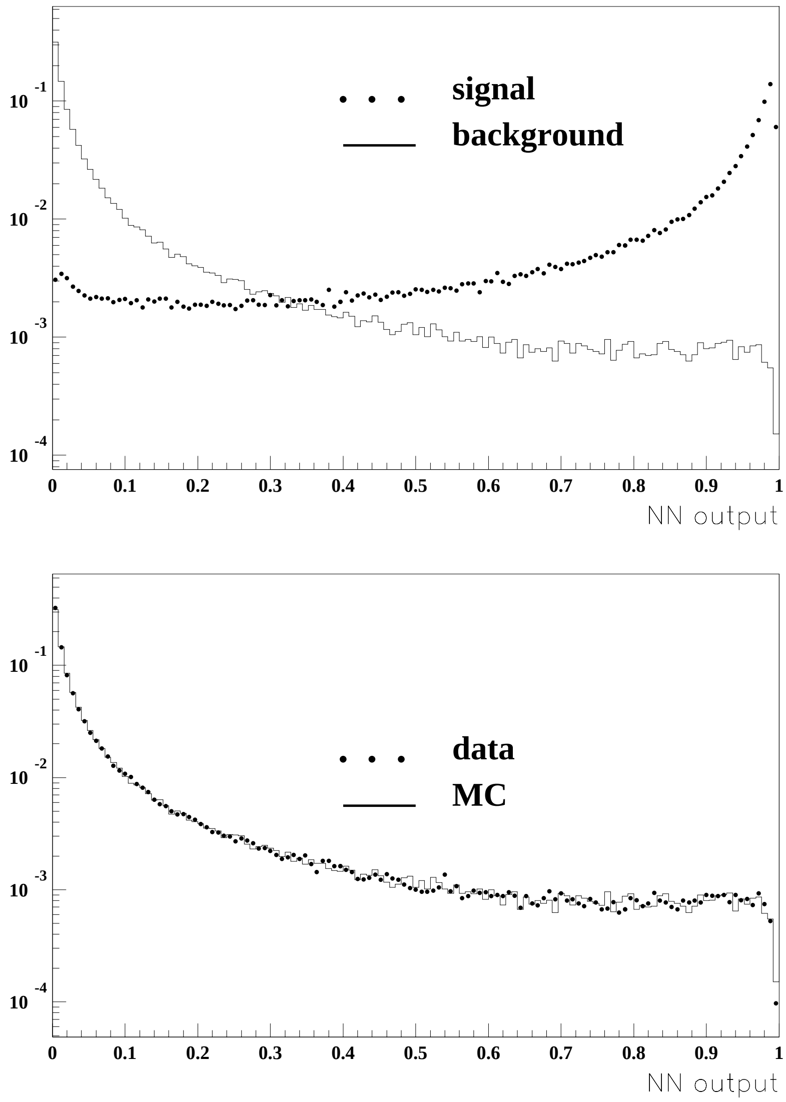

Figure 7.6: ANN output distribution for events including two coordinates silicon vertex detector information.

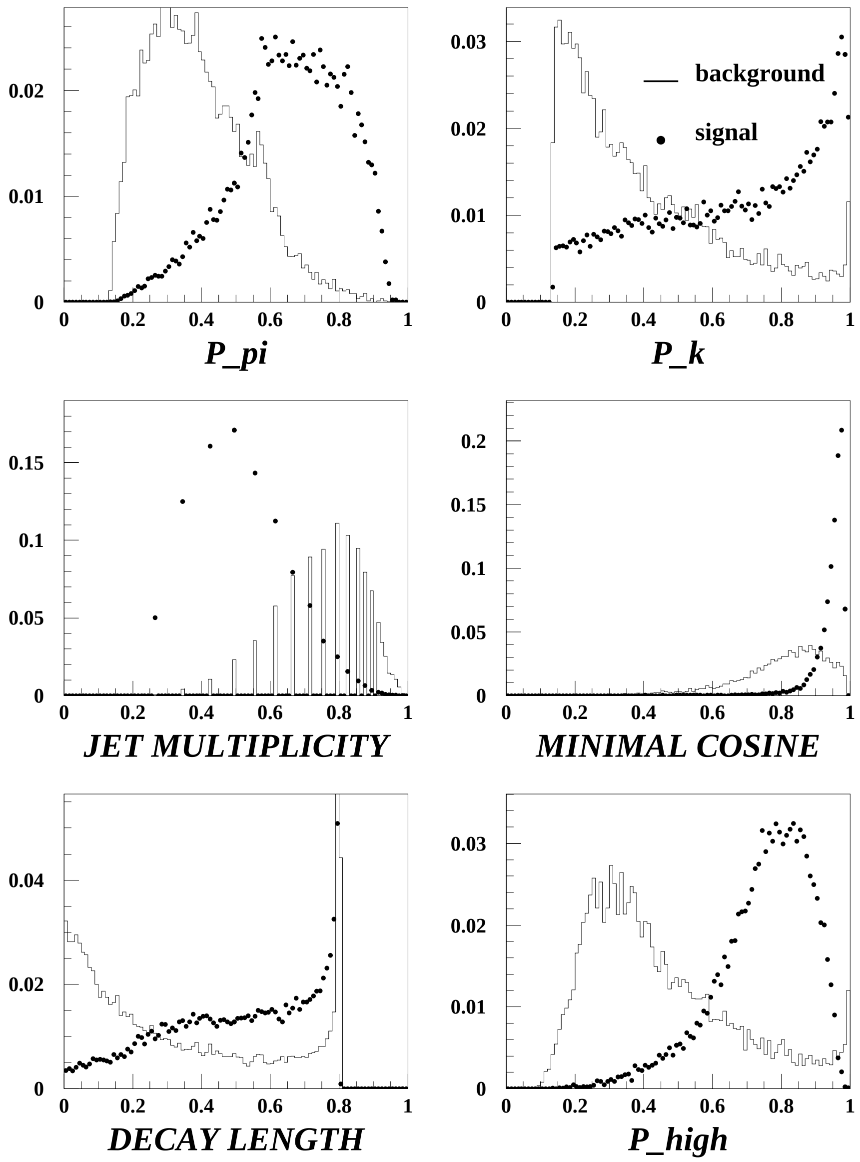

Figure 7.7: Input variables to the artificial neural network that selects $B^- \to \pi^- \pi^- K^+$ events. A comparison between $q\bar{q}$ Monte Carlo events and signal Monte Carlo events simulated without silicon microvertex detector information.

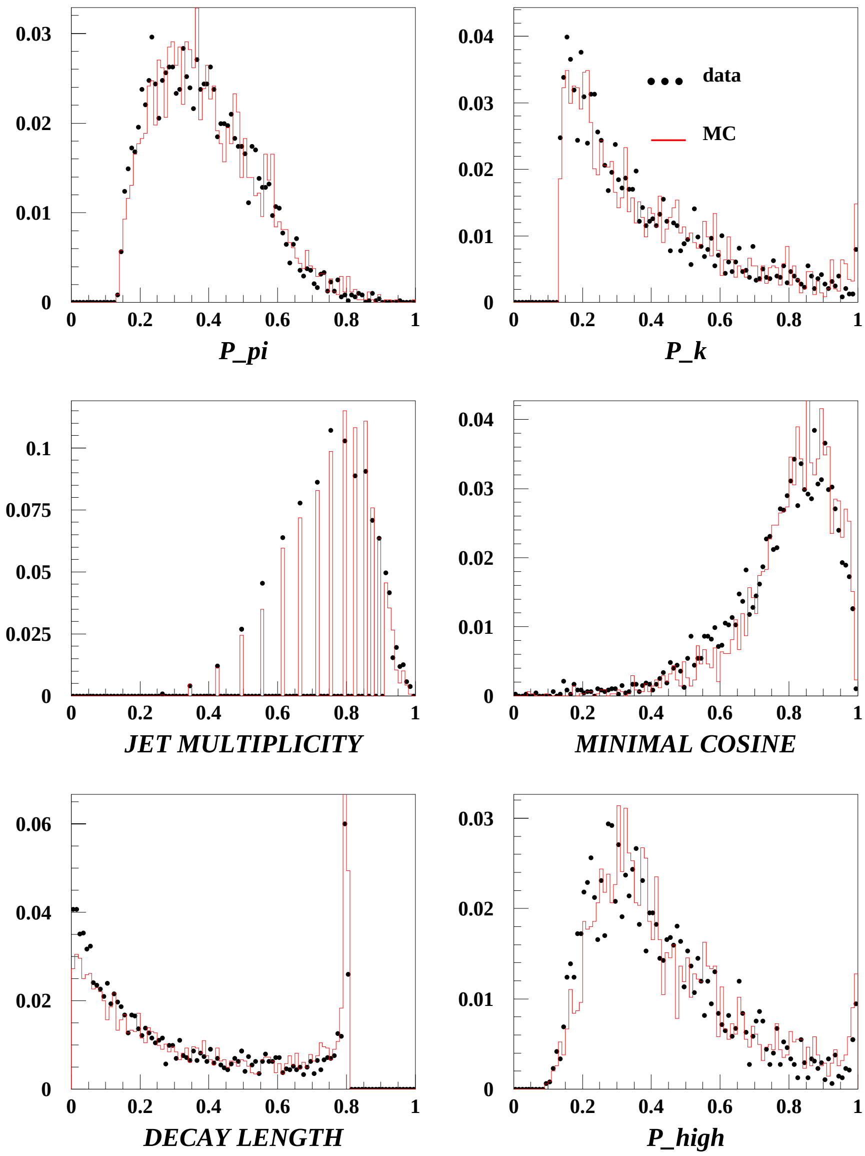

Figure 7.8: Input variables to the artificial neural network that selects $B^- \rightarrow \pi^-\pi^-K^+$ events. A comparison between $q\bar{q}$ Monte Carlo events and data without silicon microvertex detector information.

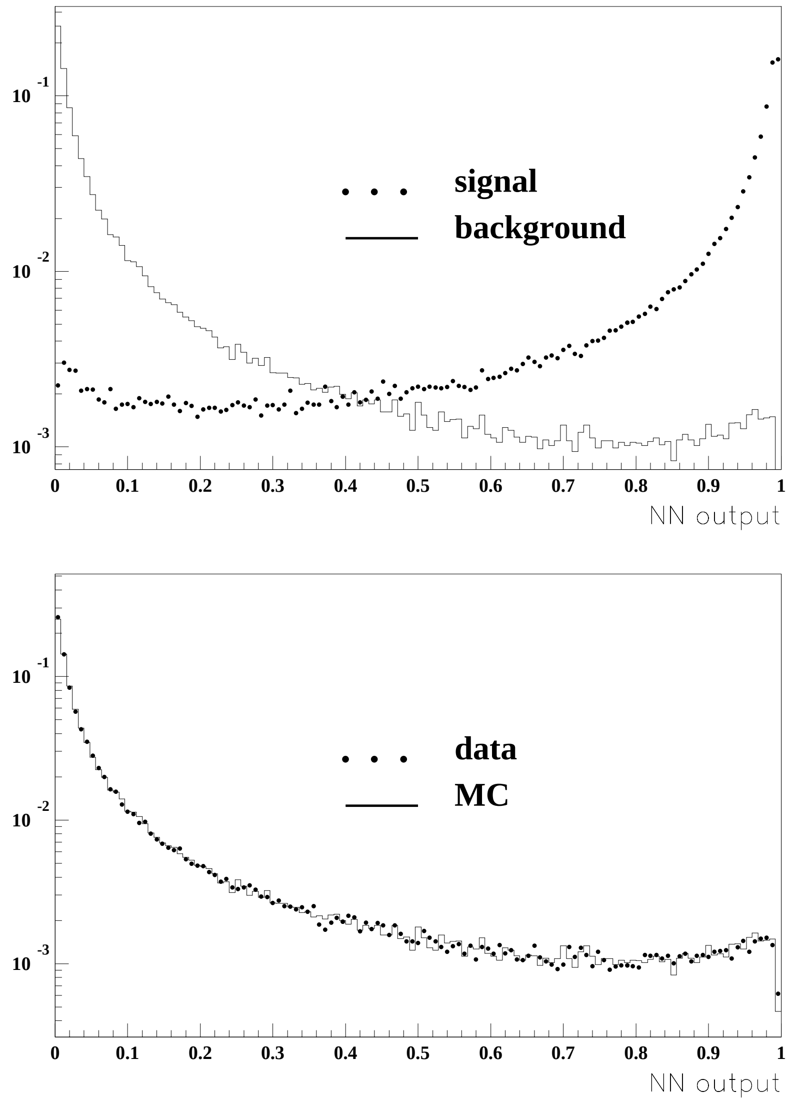

Figure 7.9: ANN output distribution for events without silicon vertex detector information.

Chapter 8

Systematic Uncertainties

Systematic uncertainties may arise from the limited accuracy with which N_B, the number of charged B mesons in the sample, is known, from the uncertainty in the simulation used to determine the efficiency and from the background estimation.

8.1 Artificial Neural Network Uncertainty

In all of the input variables to the different ANNs (figures 6.2, 7.1, 7.5, 7.8) the agreement is good between the data and the $q\bar{q}$ Monte Carlo events. However, the Monte Carlo simulation compared in those figures represents the background and is not used in setting the upper limit. The simulation used to set the limit is that of signal events and thus, signal input variables should be compared. This is not possible for the rare decays $B^- \to K_s^0 K^-$ and $B^- \to \pi^- \pi^- K^+$. Therefore, $D^{\star +}$ mesons that are relatively easy to reconstruct and have a similar event characteristics are exploited for testing the systematic uncertainty associated with the ANN selection. The search for $D^{\star +}$ mesons is via their decay into a D^0 and a π^+, where the D^0 decays via a $K^- \pi^+$. To enhance the signal to background ratio, the momentum of the $D^{\star +}$ candidate is required to be larger than 15 GeV/c; the $D^{\star +}$ decay vertex to be at least $50 \mu m$ away from the interaction point; and the helicity angle, θ^*, between the kaon momentum in the D rest frame and the D direction in the laboratory frame, to satisfy $cos\theta^* < 0.7$. Background estimation, after applying these selection criteria is done as in [20]. To avoid possible uncertainty due to the difference in the momentum spectrum of the $D^{\star +}$ products with respect to the momentum spectrum of tracks from the process $B^- \rightarrow K_s^0 K^-$ and $B^- \rightarrow \pi^-\pi^-K^+$, the dE/dx selection efficiency is reweighted as a function of the track momenta.

In order to assign a systematic uncertainty to the efficiency of the ANN, the difference between the fraction of the $D^{\star +}$ events passing the ANN cut in the data and in the $q\bar{q}$ Monte Carlo is taken.

An uncertainty of 4.9% is assigned to the ANN selection.

8.2 Modeling of dE/dx

To estimate the uncertainty arising from the modeling of the dE/dx selection criteria, the efficiency of the dE/dx cuts in Monte Carlo simulated events and in data is compared. Once again $D^{\star +}$ signal is used in the same way as for the ANN. By applying the dE/dx criteria used to select the desired event sample an uncertainty of 1.4% is obtained in the search for $B^- \rightarrow K_s^0 K^-$, and in the search for $B^- \rightarrow \pi^-\pi^-K^+$ the systematic uncertainty due to dE/dx modeling is estimated to be 3.7%.

8.3 B Hadron Lifetime

The implemented B lifetime in the Monte Carlo simulation ($1.6 \cdot 10^{-12}$ sec) does not correspond to the measured B lifetime ($(1.653 \pm 0.028) \cdot 10^{-12}$ sec). The probability to reconstruct the signal B^- meson also depends on the efficiency to reconstruct secondary vertices. The Monte Carlo was reweighted to reflect the measured B^- lifetime. The uncertainty associated with the B^- meson lifetime is estimated from the difference between the events on which the search is performed and the reweighted events.

In the search for $B^- \rightarrow K_s^0 K^-$ this uncertainty is found to be 4.3% and in the search for $B^- \rightarrow \pi^-\pi^-K^+$ an uncertainty of 3.2% is estimated.

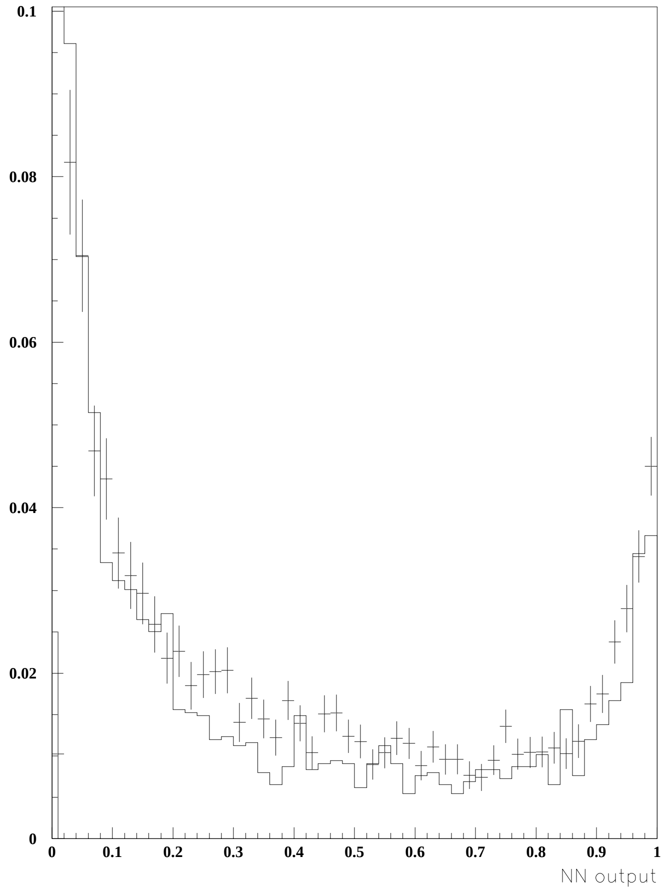

Figure 8.1: Comparison of ANN outputs for $D^{\star+}$ candidates. The solid line represents the $q\bar{q}$ Monte Carlo and the points with error bars represent the data.

8.4 Detector Modeling

The resolution of the tracking devices has an effect on the efficiency. The simulated resolutions were varied by ±10% relative to the values that optimally describe the data following the studies in [22]. The analysis is repeated and the efficiency estimation is recalculated. This source contributes an uncertainty of 2.6% in the search for $B^- \to K_s^0 K^-$ and an uncertainty of 1% in the search for $B^- \to \pi^-\pi^-K^+$.

8.5 Fragmentation Modeling

Hadronization, the transition of quarks into hadrons, is a strong interaction phenomenon which can not yet be calculated from first principles within QCD. Monte Carlo event generators are used instead which rely on phenomenological models of this process. To some extent these models can be distinguished from each other by the shape of the predicted hadron energy distribution.

8.5.1 The Peterson Model

The Peterson model of heavy quark $\mathcal{Q}$ ($\mathcal{Q} = c, b...$) fragmentation into hadrons containing $\mathcal{Q}$ follows from simple kinematical considerations as first pointed out by Bjorken and Suzuki [21].
Attaching a light antiquark $\bar{q}$ to a heavy quark $\mathcal{Q}$ (or a diquark qq for baryon production) decelerates the heavy quark in the fragmentation only slightly. Thus $\mathcal{Q}$ and $\mathcal{Q}\bar{q}$ or $\mathcal{Q}qq$ should cary almost the same energy.
The fragmentation function of this model is derived by adopting the standard quantum mechanical parton model recepie to estimate transition amplitudes. For a fast moving heavy quark $\mathcal{Q}$ fragmentation into a hadron $H = \mathcal{Q}\bar{q}$ and a light quark q, what dominates the amplitude is determined by the value of the enrgy transfered in the break up process:

$$\Delta E = E_H + E_q - E_{\mathcal{Q}} \tag{8.1}$$

$$amplitude(\mathcal{Q} \to H + q) \ \propto \ \Delta E^{-1} \tag{8.2}$$

Expanding the energies about the transverse particle masses ($m_H \simeq m_{\mathcal{Q}}$ for simplicity),

$$\Delta E = (m_{\mathcal{Q}}^2 + z^2P^2)^{1/2} + (m_q^2 + (1-z)^2P^2)^{1/2} - (m_{\mathcal{Q}}^2 + P^2)^{1/2} \tag{8.3}$$

$$\Delta E \propto \ 1 - (1/z) - (\epsilon_{\mathcal{Q}}/(1-z)) \tag{8.4}$$

Taking z^{-1} for the longitudal phase space, the following ansatz is used for the fragmentation function of a heavy quark $\mathcal{Q}$:

$$D_{\mathcal{Q}}^H(z) \ = \ \frac{N}{z[1 - 1/z - \epsilon_{\mathcal{Q}}(1-z)]^2} \tag{8.5}$$

The normalization N is fixed by summing over hadrons containing $\mathcal{Q}$,

$$\Sigma \int dz \ D^H_{/calQ(z)} = 1 \tag{8.6}$$

According to the derivation above, the parameter $\epsilon_{\mathcal{Q}}$ is $\sim m_q^2/m_{\mathcal{Q}}^2$, the ratio of the effective light - heavy-quark masses. The parameter m_q is expected to be of the order of the nonperturbative strong interaction scale $\sim (1/2 \ to \ 1)m_\rho$ which gives $\epsilon_{\mathcal{Q}} \sim (1/8 \ to 1/2)/m_{\mathcal{Q}}^2$.
The fragmentation function peaks at $z \simeq 1 - 2\epsilon_{\mathcal{Q}}$ with a width $\sim \epsilon_{\mathcal{Q}}$.

8.5.2 Model Parameter Variation

The heavy quark fragmentation was simulated using the function of Peterson [13]. The heavy-quark fragmentation model parameter (ϵ_b) was varied to change the mean scaled energy of weakly-decaying bottom hadrons within the experimental range [23]. This change results in a 0.5% change in the efficiency for the decay $B^- \rightarrow K_s^0 K^-$ and a change of 1% for the decay $B^- \rightarrow \pi^- \pi^- K^+$.
In addition, the heavy-quark fragmentation model was changed by means of reweighting to that suggested by Collins and Spiller [24] and to that of Kartvelishvili et al [25], with parameters tuned according to reference [23]. No significat change in the resulting efficiency are observed.

8.6 Summary of the Systematic Uncertainties

Table 8.1 summarizes the possible sources of the systematic uncertainty and their effect on the background and the efficiencies as discussed above.

	$B^- \to K_s^0 K^-$	$B^- \to \pi^- \pi^- K^+$
dE/dx	1.4%	3.7%
B^- lifetime	4.3%	3.2%
b-fragmentation modeling	0.5%	1%
detector modeling	2.6%	1%
ANN	4.9%	4.9%
K_s^0 identification	0.7%	—
Backgraound estimation	—	2.5%
Total systematic uncertainty	7.2%	7.5%

Table 8.1: Summary of systematic uncertainties for the two decay modes.

Chapter 9

Results

The upper limit calculation is done as described in reference [26]:
The total systematic uncertainty is $\sigma_{total}^2 = \Sigma\sigma_i^2$, where the σ_i are the uncertainties due to different sources.
U_n is the upper limit for n obsereved events, including systematic uncertainties.

$$U_n = U_{n_0}(1 + (U_{n_0} - n) \cdot \sigma^2/2) \tag{9.1}$$

U_{n_0} is the upper limit for n observed events not including systematic uncertainties:

$$U_{n_0} = \frac{N^{90}}{N_B \cdot \epsilon} \tag{9.2}$$

N^{90} is the 90% confidence level upper limit on the number of signal events.
N_B is the number of charged B mesons in the sample (see chapter 4) and ϵ is the efficiency for Monte Carlo simulated events of the signal process to survive the selection procedure.

9.1 $B^- \rightarrow K_s^0 K^-$ Results

The results of the $B^- \rightarrow K_s^0 K^-$ event selection are:

- The total efficiency for Monte Carlo simulated $B^- \rightarrow K_s^0 K^-$ events to survive the selection procedure is 4.2%.

• applying the selection to the data sample yields 0 observed events, i.e not even a single event passes the selection.

• N^{90}, the number of events that can be excluded with 90% confidence level associated with 0 observed events is 2.3.

• The total systematic uncertainty[1] for the selection is 7.2%.

From all the above the upper limit on the branching ratio of the process $B^- \to K^- K_s^0$ is:

$$\mathbf{BR(B^- \to K^- K_s^0) \leq 7.8 \cdot 10^{-5}} \quad \textit{at } 90\% \ C.L \tag{9.3}$$

9.2 $B^- \longrightarrow \pi^- \pi^- K^+$ Results

Table 9.1 summarizes the final results of the $B^- \to \pi^-\pi^- K^+$ event selection for each of the three different sample described in chapter 7.

- '3D SMVD' (for example) means - three dimensional silicon microvertex detector information is included.
- F is the fraction of the sample out of the whole data sample.
- ϵ is the total efficiency for a Monte Carlo simulated $B^- \to \pi^-\pi^- K^+$ event with the correspodent silicon detector simulation to survive the selection procedure.
- N_{BKG} is the number of expected background events.

---

[1] The complete description of how these uncertainties are obtained can be found in chapter 8

- $N_{observed}$ is the number of observed events.

- N^{90} is the number of events that can be excluded with 90% confidence level.

Sample	F	ϵ	N_{BKG}	$N_{observed}$	N^{90}
no SMVD	14%	10.5%	10	9	8
2D SMVD	24%	14.4%	9.7	14	11
no SMVD	62%	15%	99	106	27

Table 9.1: Summary of the $B^- \rightarrow \pi^-\pi^-K^+$ selection results.

9.2.1 Background Estimation

As the background to the process $B^- \rightarrow \pi^-\pi^-K^+$ is not flat, two different parameterizations of the background are tested after all selection criteria were applied, normalizing the shape to the mass side-bands ($4-5\ GeV, 5.5-6\ GeV$). Figure 9.2 shows the Invariant mass of the $\pi^-\pi^-K^+$ from top to bottom - for the sample with three dimentional silicon detector, two dimensional silicon detector and no silicon detector. The invariant mass of a combinatorial background is fitted to an exponent (plots on the left column of figure 9.2). In addition, the invariant mass is fitted to a polynomial function (the right column of figure 9.2). The systematic uncertainty associated with the background estimation is estimated from the errors on the fit parameters and the difference in the estimations from the different fits. This uncertainty is found to be 2.5%.

9.2.2 Combined Results $B^- \rightarrow \pi^-\pi^-K^+$

From combining the three different samples:

The total averaged selection efficiency - 14.3%

The total expected background - 119 events

Number of observed events in the data - 129

N^{90} - 31.8 events

The total systematic uncertainty - 7%

From all the above the upper limit on the branching ratio of the process $B^- \rightarrow \pi^-\pi^-K^+$ is:

$$\mathbf{BR(B^- \rightarrow \pi^-\pi^-K^+) \leq 2.1 \cdot 10^{-4}} \quad at\ 90\%\ C.L \tag{9.4}$$

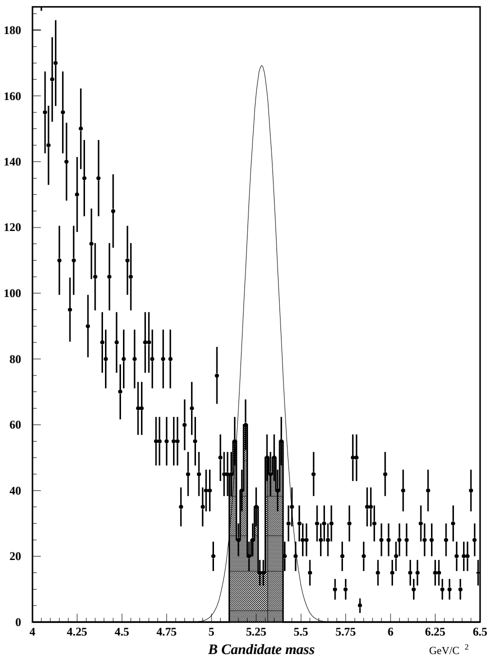

Figure 9.1: invariant mass distribution of the $\pi^-\pi^-K^+$ candidates (all three samples combined) after all selection criteria were applied. The dots represent the data, the solid line shows the expected signal shape and the dark area shows the events in the mass region 5.1-5.4 .

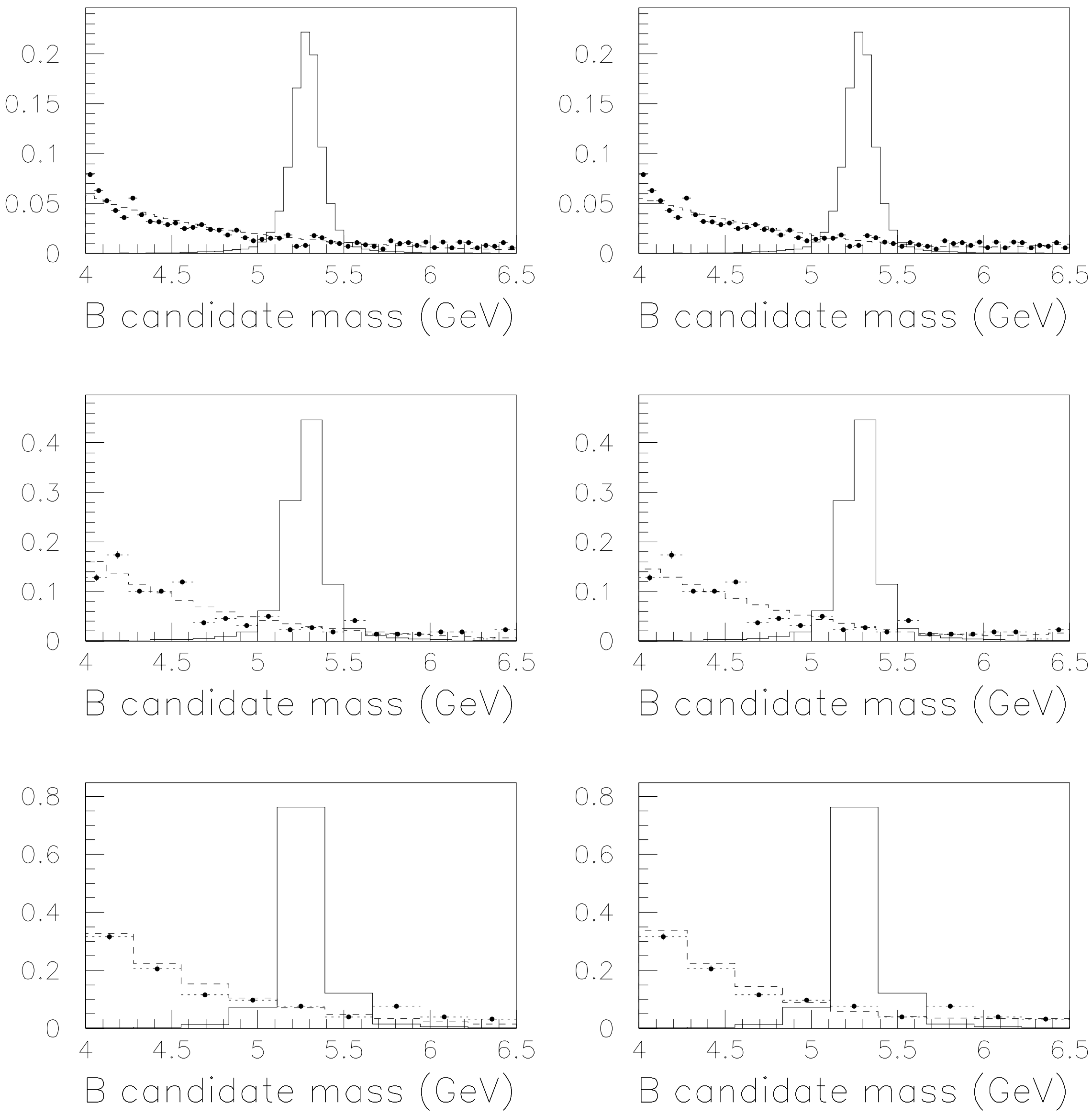

Figure 9.2: Invariant mass distribution (in GeV) of the $\pi^-\pi^-K^+$ candidates after all selection criteria were applied. The dots with the error bars represent the data, the solid line shows the expected signal shape from Monte Carlo events and the dashed line is the expected background according to the fit function described in 9.2.1.

Chapter 10

Summary

This thesis presented the search for two different modes of rare B meson decays - $B^- \rightarrow K_s^0 K^-$ and $B^- \rightarrow \pi^-\pi^-K^+$ using data collected with the OPAL detector. It is the first time that these searches are done using LEP data.
These decays are driven by the quark transitions $b \rightarrow ss\bar{d}$ and $b \rightarrow dd\bar{s}$. Within the Standard Model these decays are induced by a box-diagram and are highly suppressed. The predicted branching ratios in the Standard Model are of the order of 10^{-11} for the $ss\bar{d}$ final state and even a smaller branching ratio for the $dd\bar{s}$ final state.

The first decay channel is $B^- \rightarrow K_s^0 K^-$ where the K_s^0 candidate is reconstructed by combining pairs of opposite charged pions, and then it is combined with a kaon candidate to form a B meson candidate. A new routine for identifying K_s^0 candidates, based on an artificial neural net selection, was developed. This routine outperforms the K_s^0 identification routine of OPAL that already existed and is now being commonly used in the collaboration. The reconstruction of the B meson candidate, apart from using hard cuts on different one-dimensional parameters, is also based on an artificial neural net selection designed to select the specific decay while rejecting background events.

The second decay that is analysed is the $B^- \rightarrow \pi^-\pi^-K^+$. These analysis is divided into three different samples of data and Monte Carlo events due to its high sensitivity to the vertex reconstruction using the silicon microvertex

detector. After analysing the three different samples separately (no silicon microvertex detector information, two dimensions silicon microvertex detector information and three dimensions silicon nicrovertex detector information) using a set of one-dimensional cuts and an artificial neural network that was trained separately for each of the samples, they are combined in order to obtain the upper limit on the branching ratio of this decay.
In both decay channels no specific processes are found to be a dominant background and the combinatorial background is rejected by cutting on parameters like energy loss, reconstracted B meson mass, momentum,decay length and decay angles.

In both decay channels no evidence for signal is found.
The upper limits on the branching ratios of these decays obtained here are as follows:

$$\mathcal{BR}(B^- \to K_s^0 K^-) \leq 7.8 \cdot 10^{-5} \tag{10.1}$$

$$\mathcal{BR}(B^- \to \pi^- \pi^- K^+) \leq 2.1 \cdot 10^{-4} \tag{10.2}$$

These results are consistent with other measurements done with other experiments. The CLEO and BaBar collaborations give lower upper limits due to higher statictics.
The upper limits given by these analyses do not provide unexpected results according to the theoretical predictions either within the Standard Model or beyond it. In order to confirm or contradict the theoretical predictions more statistics is needed. It is hoped to improve the results of this search and the searches for other rare B meson decays in the future, using data collected in B-factories and in the LHC experiments.

Bibliography

[1] K. Hagiwara *et al*, Phys. Rev. D 66, 010001 (2002).

[2] S.Fajfer, P.Singer, Phys.Rev. D62(2000) 117702; S.Fajfer, P.Singer, Nucl. Phys. Proc.Suppl. 93(2001) 103-106; K. Huitu, C.-D. Lü, P.singer, D.-X. Zhang, Phys. Lett. B445(1999) 394-398; K. Huitu, C.-D. Lü, P.singer, D.-X. Zhang, Phys. Rev. Lett. 81(1998) 4313-4316.

[3] OPAL collaboration G. Abbiendi *et al*, Phys. Lett. B467(2000) 233-242.

[4] K. Abe *et al*, BELLE Collaboration, hep-ex/0201007.

[5] BaBar Collaboration, SLAC-PUB-8996, proceedings of ICFP2001.

[6] CLEO Collaboration, Phys. Rev. Lett77:4503-4507, 1996.

[7] Belle Collaboration, hep-ex/0207003, to appear in proc. for FPCP, May 16-18 2002, Philadelphia, USA.

[8] P. Billoir Nucl. Instrum. Meth. 225(1984).

[9] http://opalinfo.cern.ch/opal/manuals/oprimer/oprimer.html

[10] JADE Collaboration, W. Bartel *et al*, Z. Phys **C 33** (1986) 23;
JADE Collaboration, S. Bethke *etal*, Phys. Lett. **B 213** (1988) 235.

[11] T. Sjöstrand, Comp. Phys. Comm. **82** (1994) 74;
T. Sjöstrand, Comp. Phys. Comm. **39** (1986) 347;
M. Bengtsson and T. Sjöstrand, Comp. Phys. Comm. **43** (1987) 367;
T. Sjöstrand, Int. J. of Mod. Phys. **A 3** (1988) 751.

[12] J. Allison *et al*, Nucl. Instr. Meth. **A 317** (1992) 47.

[13] C. Peterson *et al*, Phys. Rev. **D 27** (1983) 105.

[14] L. Lonnblad, C. Peterson and T. Rognvaldsson, Comp. Phys. Comm. **70** (1992) 167.

[15] C. Peterson and T. Rognvaldsson, LU TP 91-23, "An introduction to ANN"

[16] Rumelhart D.E., McClelland J.L., eds. Parallel Distributed Processing, Vol. 1 and Vol. 2, MIT Press, Massachusetts, 1986.

[17] Y. Rozen, S. Moed, OPAL TN-669, October 2000.

[18] OPAL Collaboration, R. Akers *et al CERN-PPE/95-024 Z. Phys. C67 (1995) 389-401.*

[19] OPAL Collaboration, R. Akers et al, Z. Phys. **C 66** *(1995) 19.*

[20] 'Measurement of the Production Rate of Charm Quark Pairs from Gluons in Hadronic Z^0 Decays', OPAL Collaboration, G. Abbiendi [et al, CERN-EP/99-089.

[21] Bjorken, Phys. Rev. D 17, 171 (1978).

[22] OPAL Collaboration, G. Abbiendi *et al*, Eur. Phys. J. **C 8** (1999) 217.

[23] *Inclusive Analysis of the b Quark Fragmentation Function in Z Decays at LEP* hep-ex/0210031, submitted to Eur.Phys.J. C.

[24] P. Collins and T. Spiller, J. Phys. **G 11** (1985) 1289.

[25] V.G. Kartvelishvili, A.K. Likehoded and V.A. Petrov, Phys. Lett. **B 78** (1978) 615.

[26] R.D. Cousins and V.L. Highland, Nucl. Instr. Meth **A 320** (1992) 331.